POLITECNICO DI TORINO

Collegio di Ingegneria Chimica e dei Materiali

Master of Science Course
in Materials Engineering for Industry 4.0

Master of Science Thesis

Impact of GaAsSb Capping Layer on the performance of InAs Quantum Dots Solar Cells

Politecnico
di Torino

Tutors

University Tutor
Prof. Micaela Castellino

External Tutor
Prof. Jose María Ulloa

Candidate

Enrico Squiccimarro

October 2024

To my family, for their unconditional love and support.

To my love, for her constant presence and encouragement.

And to everyone who has supported me along this journey.

Acknowledgments

I would like to express my deepest gratitude to Professor Jose María Ulloa for the invaluable opportunities he has provided and for imparting his passion for this field to me. His guidance and encouragement have been instrumental in shaping my academic journey and inspiring my research.

My heartfelt thanks go to Malte Schwarz for his unwavering commitment, patience, and availability throughout this project. His support has been essential in overcoming numerous challenges and achieving the project's objectives.

I am also profoundly grateful to Professor Micaela Castellino for her steadfast support. Her encouragement and insightful advice have been crucial throughout the course of my research.

I extend my sincere thanks to Professor Marco Sangermano for his constant presence and mentorship during my Erasmus project, which has been one of the most enriching experiences of my life. His support has had a significant impact on both my personal and professional growth.

I would like to thank Sergio Catalán Gómez for his positivity, which has been a source of motivation and encouragement. Additionally, I am grateful to the technical staff at ISOM for their invaluable assistance and support throughout this project.

Abstract

Quantum dot solar cells (QDSCs), based on semiconductor materials, hold potential for improved performance by capturing a broader portion of the solar spectrum. In particular, InAs quantum dots (QDs) covered with a thin GaAsSb capping layer are promising for enhancing GaAs solar cell efficiency. Despite their advantages over standard InAs QDs, the carrier transport and recombination mechanisms in these modified QD structures are not yet fully understood. This Master Thesis conducts an optoelectronic analysis of solar cells containing various $GaAs_{1-x}Sb_x$/InAs QD structures to understand the transport and recombination mechanisms and evaluate performance under diverse conditions.

The study is divided into two parts. Firstly, the properties of solar cells at room temperature are analysed, focusing on the effect of Sb concentration in the capping layer on recombination mechanisms, absorption edges, energy conversion efficiency, and unintentional doping concentrations. The second phase involves temperature-dependent measurements from 330 K to 25 K to explore carrier dynamics and efficiency loss mechanisms. Various illumination conditions are assessed. Current – voltage (IV) characteristics were measured under dark conditions, 1 sun AM1.5G, and 2 suns AM1.5G illumination. IV measurements under 1 sun AM1.5G with a GaAs filter were also performed to isolate the contribution of the multilayers chosen samples made up by 10 QDs layers in the GaAs p-i-n junction. The results indicate that low concentrations of Sb can enhance efficiency, while high concentrations of Sb can cause non-radiative recombination losses. The study also shows that transport phenomena vary with temperature. Additionally, QD presence and their specific band structures, influenced by the capping layer composition, lead to higher efficiencies under increased power due to saturation of the nanostructures.

This comprehensive optoelectronic analysis allows to assess QDSCs for applications as single junction solar cells, multi-junction solar cells, concentrator solar cells and in-space devices, where high efficiency, lightweight design, and resilience to extreme conditions are critical.

Table of Contents

1. Introduction and motivation

This chapter begins with an examination of the evolution of the energy transition, highlighting the shift away from fossil fuels towards sustainable alternatives such as solar energy. Subsequently, the chapter delves into the field of solar cells, discussing advancements in improving solar cell conversion efficiency.

1.1 Energy transition: from fossil fuels to solar energy

In 2003, the Nobel prize winner, Professor Richard Errett Smalley, outlined humanity's top ten challenges for the ensuing fifty years during a lecture at Rice University [1]. His list included among others:

- Energy
- Water
- Food
- Environment
- Poverty
- Terrorism and war
- Disease
- Education
- Democracy
- Population.

It is noteworthy that energy occupies the first position on the list, despite the greater attention often given by media and public figures to the other topics. However, making energy a priority is understandable, as many of the other challenges, notably environmental concerns, are linked to energy [2].

Both the international community and national governments recognize the imperative need for substantial efforts in addressing environmental issues. The Kyoto Protocol in 1997 [3] stands out as one of the major attempts in this regard, which commits to reduce the emissions of six greenhouse gases: methane (CH_4), carbon dioxide (CO_2), hydrofluorocarbons (HFCs), nitrous oxide (N_2O) sulphur hexafluoride (SF_6) and perfluorocarbons (PFCs). Subsequently, at COP 21 in Paris, in 2015 [4], an agreement was established to address climate change and to speed up and enhance the efforts and investments required for a sustainable, low-carbon future. The goal of the Paris Agreement is the transformation of the global energy sector from fossil-based to zero-carbon sources by the second half of this century (2050), aiming to mitigate climate

change, reduce energy-related CO_2 emissions, and limiting the rise in global temperatures to 1.5°C of pre-industrial levels [5-6].

For more than a century, economies have relied on fossil fuels such as oil, coal and natural gas, which currently provide approximately 80% of the world's total energy supply [7]. In *Figure 1.1* the fossil fuels consumption over a fifty-seven-year period is shown. Furthermore, the values corresponding to terawatt-hours consumed by energy source in the year of 2010 are highlighted [8]. Despite the policy efforts mentioned above, consumption of fossil fuels is still increasing. In response, governments and scientists across numerous nations are actively seeking new energy sources, particularly those categorized as "*alternative energy*" due to their environmental sustainability.

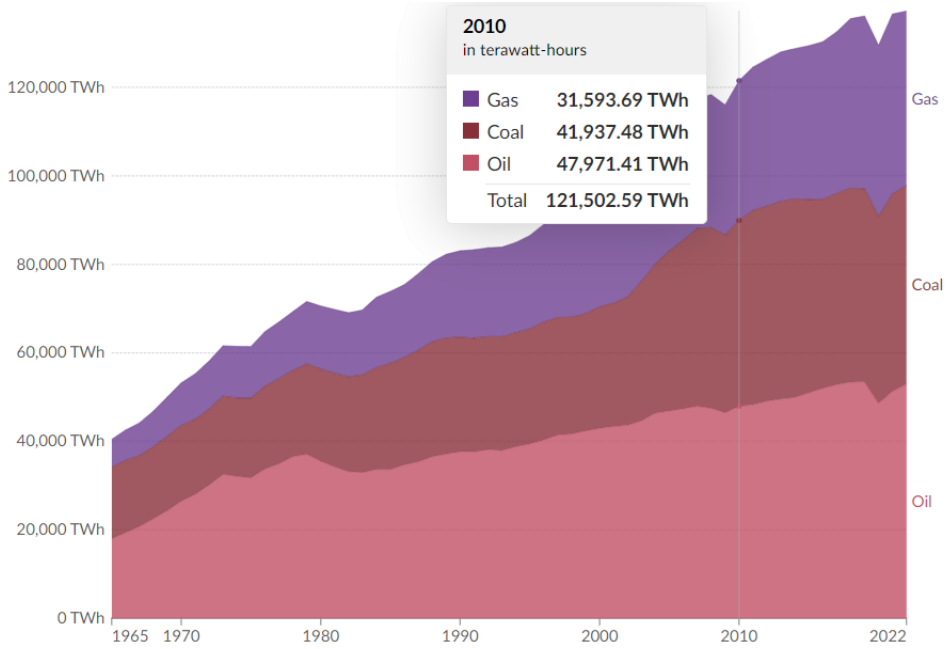

Figure 1. 1: *Fossil fuel energy consumption given in terawatt-hours (TWh) from 1965 to 2022 for three major fossil fuels [8].*

Various forms of *alternative energy* exist, such as nuclear, wind, hydroelectric, geothermal and solar power. Hydropower and nuclear power are fundamental to low-carbon electricity generation, collectively accounting for three-quarters of global low-carbon electricity production [9]. Nevertheless, nuclear power faces limitations due to its complex technology and associated risks. Similarly, hydroelectric power is limited by geographical factors such as the presence of rivers and rainfall patterns, which can impact on local ecosystems and climates.

In contrast, solar energy is used through photovoltaics to generate electricity, with several advantages. It features simpler technology, improved safety, negligible gas emissions, geographical versatility, and abundant resources [10]. All these advantages ensure that solar energy has significant potential as a future energy solution.

1.2 Market for solar energy

The use of solar energy began in niche markets, supplying electricity to applications with few alternatives, such as in space and remote locations. Over time, cumulative investments and sales, supported by favourable policies, have reduced its cost by nearly three orders of magnitude, making solar energy one of the most promising alternatives to replace fossil fuels [11]. Solar power is produced using two main methods: Solar Photovoltaic (PV) and Concentrated Solar Power (CSP). The former employs electronic devices, known as solar cells, to directly convert sunlight into electricity and represents one of the most rapidly advancing technologies in renewable energy. At the end of 2020, the worldwide installed capacity of solar PV reached 710 GW, with approximatively 125 GW of new solar PV capacity added that year [12]. On the other hand, the CSP uses mirrors to focus solar rays, heating fluids to produce steam that powers turbines for electricity generation in large-scale power plants. At the end of 2020, the global installed CSP approached 7 GW, representing a fivefold increase since 2010 [12]. Although CSP has the great advantage of storing energy over solar PV, technological simplicity and market size have contributed to the dominance of PV over CSP, as shown in *Figure 1.2* [13].

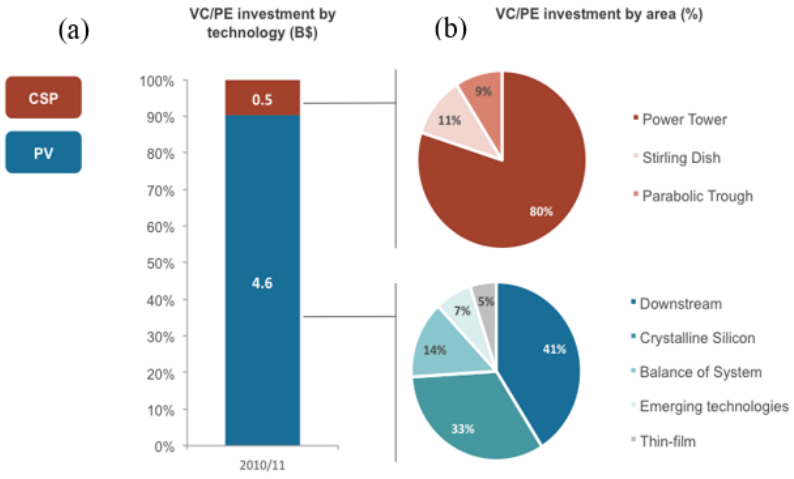

Figure 1. 2: *Venture Capital (VP) and Private Equity (PE) investments in PV and CSP by technology (a) and by area (b) in 2010/2011 [13].*

Research and development efforts on photovoltaic technologies gradually decreased the cost per watt. As illustrated in *Figure 1.3*, solar photovoltaics accounted for 1% of electricity generation in 2015, but this value is projected to rise to 22% by 2050 [14]. A study by the National Renewable Energy Laboratory (NREL) projected that 40% of all electricity generation in the US could come from solar energy by 2035 [15], making the phantom energy transition possible.

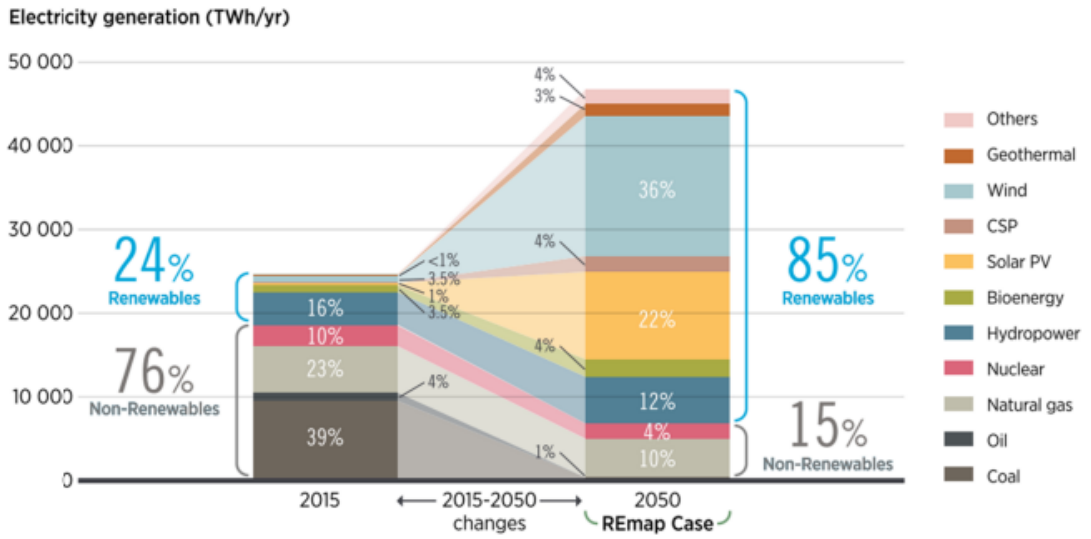

Figure 1. 3: *Electricity generation in TWh per year per energy sources [14].*

1.3 Efficiency as the keystone of the solar cells evolution

Light is converted into electric current through a process called *Photovoltaic effect* [16]. The photovoltaic effect is the process where certain materials generate electricity when exposed to light. When photons (light particles) hit the material, they can excite electrons, leading to the generation of electrical voltage and current. This principle is the basis for solar cells, which are devices that directly convert light from the sun into electrical energy through the photovoltaic effect. A more detailed description on this process is given in [17]. The photovoltaic effect was discovered for the first time in 1839 by the French physicist, Alexandre Edmound Becquerel [16]. Several decades later, in 1873, English engineer Willoughby Smith discovered the photoconductivity of selenium while testing materials for underwater telegraph cables. In 1883, American inventor Charles Fritts created the first solar cell from selenium [18].

Nowadays, based on the different operational processes, as well as the materials used, photovoltaic cells are divided into three categories: *First Generation Solar Cells, Second Generation Solar Cells* and *Third Generation Solar Cells* [19].

First Generation Solar Cells

The first-generation solar cells are made using silicon wafers. This is the oldest and most widely used technology. The silicon wafer-based technology is further divided into two subgroups [20]: single/mono-crystalline Silicon solar cells and poly/multi-crystalline Silicon solar cells.

Second Generation Solar Cells – Thin Film Solar Cells

Second-generation solar cells include the advancement of first-generation photovoltaic cell technology, along with the development of thin-film photovoltaic cell technology using materials such as amorphous Silicon (a-Si), microcrystalline Silicon (μc-Si), Cadmium Telluride / Cadmium Sulphide (CdTe / CdS) cells and Copper Indium Gallium Selenide (CIGS) [20-21]. While thin films are cheaper than traditional first-generation Silicon devices, they typically suffer losses due to lower film quality [22].

Third Generation Solar Cells

Dye-sensitized solar cells (DSSCs) were the first reported by Grätzel [23] to belong to the third-generation solar cells. This subgroup has expanded to include organic photovoltaics (OPV) or organic solar cells (OSCs), perovskite solar cells (PSCs) and quantum dot solar cells (QDSCs) [24]. The opportunity for improvement is further enhanced by multi junction solar cells (MJSCs), that combine the properties of organic and inorganic materials [24]. These three categories are summarized in *Figure 1.4.*

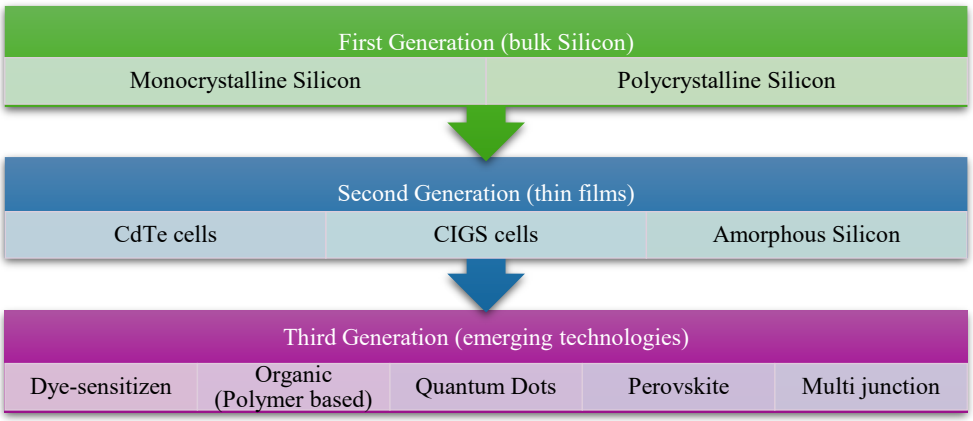

Figure 1. 4: *Solar cell generations: according to [20][21][22][24].*

As depicted in *Figure 1.5* the evolution of solar cell technologies is continually driven by the quest to increase their conversion efficiency. The conversion efficiency in solar cells is the most crucial parameter and it must be particularly considered in energy applications. Nowadays, the goal imposed on PV- technologies is to surpass 50% of conversion efficiency [15], which means that half of the energy carried with the solar light should be converted into electric power.

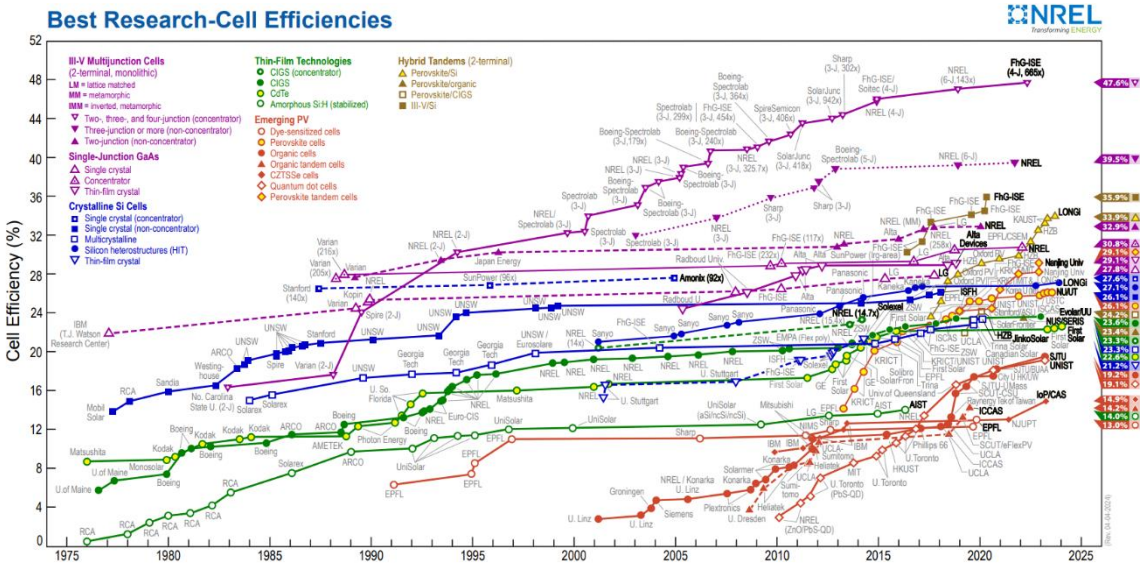

Figure 1. 5: *Progression in terms of efficiency of all solar cells created and produced, with results that have been certified by associated entities [25].*

Figure 1.5 illustrates the evolving efficiency trends of various families of solar cells over time, highlighting the significant advancements in GaAs single junction and III-V multi junction cells. Currently, these cells exhibit efficiencies of approximately 28% and 40%, respectively,

with a clear upward trajectory in their performance [25]. Further efficiency enhancements are achieved through the use of concentrator solar cells (CSCs). These systems employ lenses and reflectors to increase the intensity of sunlight incident on the photovoltaic cells, thereby enhancing the overall yield of the PV system [26]. Consequently, efficiency levels can reach up to ~ 31% for GaAs single-junction cells and ~ 48% for III-V multi junction cells.

1.4 Novel strategies to enhance efficiency

Nowadays, the most common architecture for solar cells is the single-junction solar cell (SJSC), where the junction is formed in a single material. This design is more widespread due to its easier fabrication and lower cost. However, SJSCs can absorb only a portion of the solar spectrum because they are made of a single type of semiconductor material with a specific bandgap energy (E_g). The bandgap is the energy difference between two specific energy levels in a semiconductor material. Only photons with energy equal to or greater than this bandgap can excite electrons and generate electricity. Photons with energy lower than the bandgap pass through the material without being absorbed. As a result, single-junction solar cells can only effectively convert a limited range of the solar spectrum into electricity. SJSCs suffer also from thermal losses for photons with energy much higher than the bandgap [27].

To address these issues, cells with multiple layers, known as multi-junction solar cells, are currently one of the most successful concepts, overcoming the efficiency limit [22] of single junction solar cells.

The basic principle of MJSCs is the synergic use of cells with different bandgaps to absorb distinct parts of the solar spectrum. Monolithically stacked III–V multi-junction solar cells have reached efficiencies of 38.8% under the AM1.5G and 35.1% under AM0 for space applications [27]. In *Figure 1.6* the concept of a MJSC is illustrated.

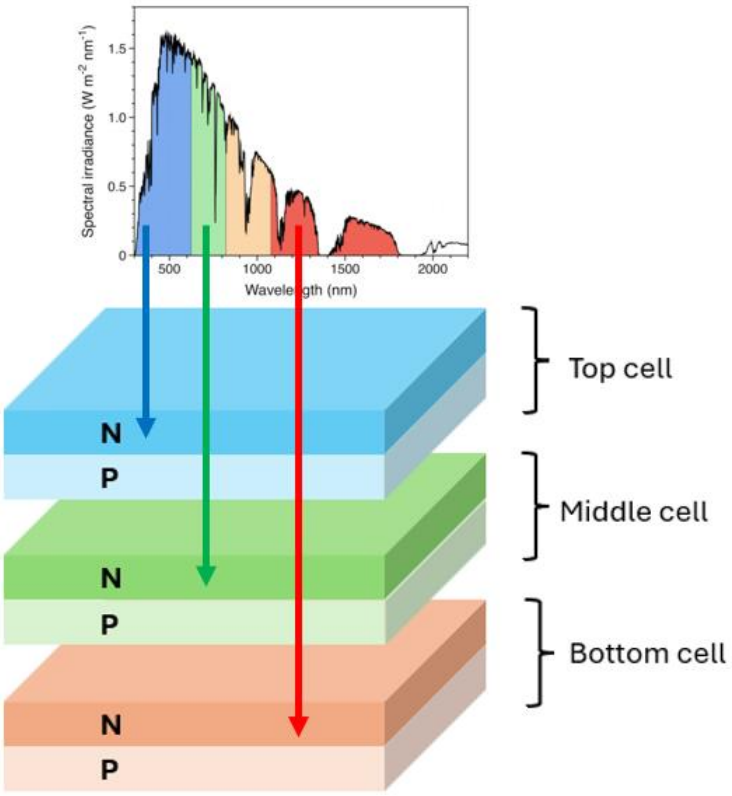

Figure 1. 6: *Schematic structure for a triple-junction solar cell (below). Photons at different energy, coming from different spectral ranges of the solar spectrum (on top) are absorbed by the three sub-cells.*

The current standard multi-junction solar cell design combines three sub-cells made of Ge (E_g = 0.66 eV and λ = 1878 nm), GaAs (E_g = 1.42 eV and λ = 873 nm) and InGaP (E_g = 1.9 eV and λ = 652) from bottom to top. This design fails to utilize the full potential of Sun spectrum. It has been reported that the bottom cell generates excess photocurrent, up to 60% more than the top two sub-cells [28]. This surplus current is dissipated as heat, leading to performance degradation. Therefore, increasing the photocurrent generated in the other sub-cells is required for current matching [29]. Moreover, in order to address thermal losses and to extend the absorption towards infrared photons, in both the GaAs SJSCs and the GaAs sub-cell in the MJSCs, new approaches are necessary.

One promising approach involves embedding InAs quantum dots (QDs) within the GaAs cell or sub-cell [28]. This extends the absorption range from the GaAs cell and thereby utilizes the excess photocurrent otherwise lost through the Ge sub-cell. Quantum dots, due to their tuneable bandgap, can effectively absorb photons across a broader spectrum, enhancing the overall efficiency of the solar cell [30].

However, the use of QDs entails some drawbacks. Firstly, carrier localization within the nanostructures leads to low extraction efficiency due to a short radiative lifetime. Secondly, embedding QDs in a barrier material results in strain accumulation, which limits the number of QD layers that can be stacked and therefore the relative absorption. Moreover, strain generation at the QD/barrier material interface causes limitations in the QD dimensions, rendering effective bandgap tuning difficult [30].

These issues can be addressed by capping the QDs with GaAsSb. The capping layer (CL) further extends the absorption range to longer wavelengths, but it also increases carrier lifetime and extraction efficiency due to a modification in the electronic band structure of the barrier material [30]. Further discussions on the physics of QDs and capping layer strategies are provided in Chapter 3.

In *Figure 1.7* the solar spectrum is coupled with the absorption ranges of three different materials: GaAs, InAs QDs and InAs QDs capped with functional layers.

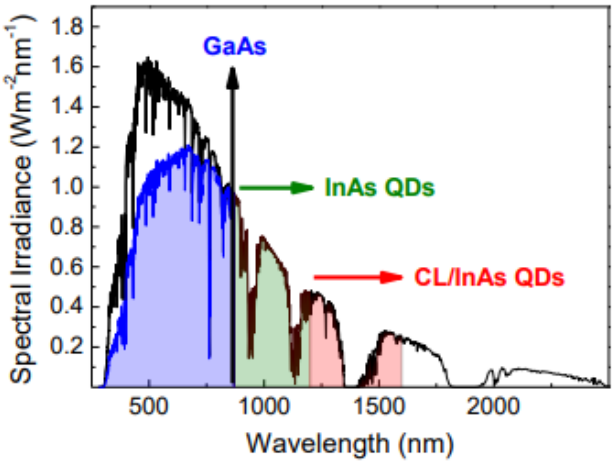

Figure 1. 7: *The AM1.5G solar spectrum (black curve) illustrates the light converted into electricity by GaAs (blue-shaded curve). The shaded region beyond GaAs absorption edge denotes the extended range of the solar spectrum that can be harnessed by InAs QDs (green) and InAs QDs capped with a CL (red) [30].*

From this graph, it is possible to infer the potential of coupling these three materials in an advanced solar cell.

1.5 Solar cells for space applications

Due to the high fabrication costs associated with III–V materials, advanced solar cells are used primarily in high-end fields, such as aerospace and military applications [14,31]. The unique

environment of space presents specific challenges for solar cell technology with the need for high efficiencies, making Silicon SJSC not suitable.

Since the launch of satellite Vanguard by NASA, photovoltaic systems have provided a primary power source in aerospace applications [32]. Numerous upcoming missions require advanced solar cells and array technologies to meet their power demands. These technologies need to offer high efficiency, low mass, compact storage, and high reliability. Some missions may prioritize certain features over others based on their specific requirements and environments. For instance, Near-Sun missions require technologies that can handle high solar intensities and maintain performances at elevated temperatures. Missions to the Moon, Mars, and asteroids need solar technologies that deliver high specific power and efficiency at moderate light levels and temperatures. The missions to outer planets require new photovoltaic technologies capable of generating power at extremely low light levels and temperatures [32-33].

Lastly, but equally important are the space power systems for use in low-Earth orbits (LEO). In this case, the photovoltaic systems experience a variety of harsh environmental conditions including atomic oxygen, radiation, thermal cycling, and debris impact. Each of these can adversely affect the performance of the space power system [34]. Regarding the thermal cycles in LEO, being shadowed for 30 min during the 90-minute orbit, it causes a temperature swing from 60 to -150 °C. In 1 year, satellites in LEO can experience 9000 of these temperature cycles [35]. Hence, the necessity to develop systems capable of operating under the varying light and temperature conditions in low-Earth orbit is crucial for ensuring consistent energy supply and optimal performance. Quantum dot solar cells offer significant potential for enhancing the performance and efficiency of space power systems. Their unique properties, such as high efficiency, flexibility, and lightweight design, make them suitable for the demanding conditions of space [36-37].

1.6 Objective of the thesis

The main objective pursued in this Master Thesis consists in an optoelectronic analysis of GaAs solar cells containing InAs quantum dots with different compositions for $GaAs_{1-x}Sb_x$ capping layer, with the objective of improving understanding of transport and recombination mechanisms in these quantum dots solar cells as well as their performance under different conditions.

This analysis is divided into two main phases, aiming to understand how the presence of quantum dots and the composition of the capping layer influences the solar cells.

First, the properties of the cells are examined at room temperature through, photocurrent spectroscopy, capacitance – voltage profiling and current – voltage curves under dark and illuminated conditions. The influence of the Sb concentration in the capping layer on the absorption and on the energy conversion efficiency of each cell is studied. This analysis helps to identify variations in cell performance and provides a better understanding of the physical mechanisms that govern the behaviour of QDSCs. In addition, a characterization regarding unintentional doping concentration is performed. It provides an indication of the effect of QDs and CLs on the concentrations of defect states.

Secondly, the solar cells are analysed, through current – voltage measurements, at cryogenic temperatures to examine the carrier dynamics processes and efficiency loss mechanisms in each sample in more details. Measurements under dark conditions are carried out to further understand the influence of Sb on carrier dynamic and recombination mechanisms. Moreover, 1 sun AM1.5G and 2 suns AM1.5G as function of the temperature are studied to discuss how the efficiency of these cells varies with temperature and illumination conditions.

The combined optoelectronic analyses carried out in this thesis are essential for evaluating the potential applicability of these systems in extreme environments, such as space, where illumination and temperature conditions can significantly differ from terrestrial ones. Studying the performance of QDSCs under different levels of illumination and thermal conditions allows for determining the robustness and stability of the cells and identifying the most promising CL configurations for applications in different operating environments, thus contributing to the advancement of next-generation photovoltaic technologies.

2. Basics of solar cells

This chapter introduces solar cells, emphasizing the essential physics behind their functionality. Conventional solar cells are analysed, highlighting the most important parameters used to indicate solar cell performance, such as open-circuit voltage, short-circuit voltage, fill factor, efficiency, and unintentional doping concentration.

2.1 Semiconductor band structure

Semiconductors are materials with a crystalline structure that gives them unique electronic properties, based on their energy band structures. The structure of semiconductors includes two main bands: the valence band and the conduction band. In the valence band, electrons are tightly bound to the atoms of the crystal lattice and cannot move freely to conduct electricity. Instead, the conduction band, situated at a higher energy level, contains vacant electronic states that are available for electron movement. The difference between the maximum energy in the valence band (VB) and the minimum energy in the conduction band (CB) is known as the energy gap or band gap. An illustration of the band structure of a semiconductor is given in *Figure 2.1.* By modifying this structure through the doping process, which introduces controlled impurities, it is possible to create materials with an excess of electrons (n-type) or with electron deficiencies known as holes (p-type), thereby determining the electrical behaviour of the semiconductor [17,38].

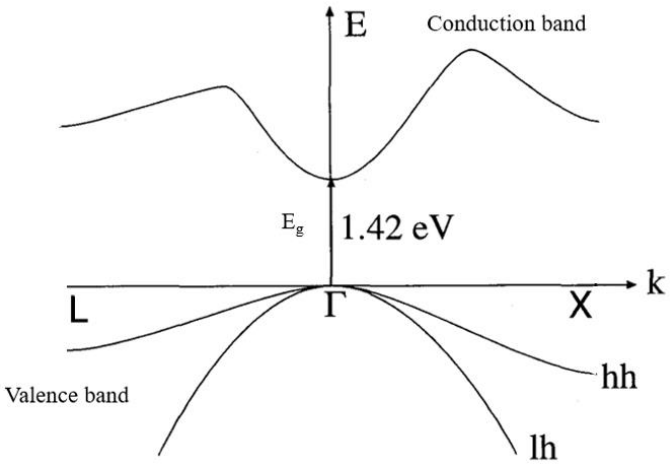

Figure 2. 1: *Simplified band diagram for GaAs at 300 K. The energy of the electron E is plotted as a function of crystal momentum k for the various bands (hh: heavy holes, lh: light holes) and directions in the crystal X and L. The energy gap (E_g) of GaAs, at room temperature, is indicated [39].*

2.2 The p-n junction

When introducing the operating principle of a solar cell, it is useful to start with the simplest case, which is the p-n junction. These junctions are realized with n- and p-type adjacent semiconductors, with different doping concentrations. Upon formation of a p–n junction, the concentration gradient between the two regions creates a diffusive current flow (diffusion current) where holes diffuse from the p-type semiconductor to the n-type semiconductor, and electrons diffuse in the opposite direction, as depicted in *Figure 2.2(a)*. The interface region between n- and p-type materials is thus depleted of free charges, forming what is called the depletion region or the space-charge region (SCR). An illustration of the p-n junction once the SCR is set up is given in *Figure 2.2(b).* The electric field created by the fixed charges contributes to balance the diffusion current, promoting an opposite drift current that leads to thermal equilibrium. The difference in electrostatic potential formed between p- and n-type semiconductors at thermal equilibrium is called the built-in potential (V_{bi}) [17,38].

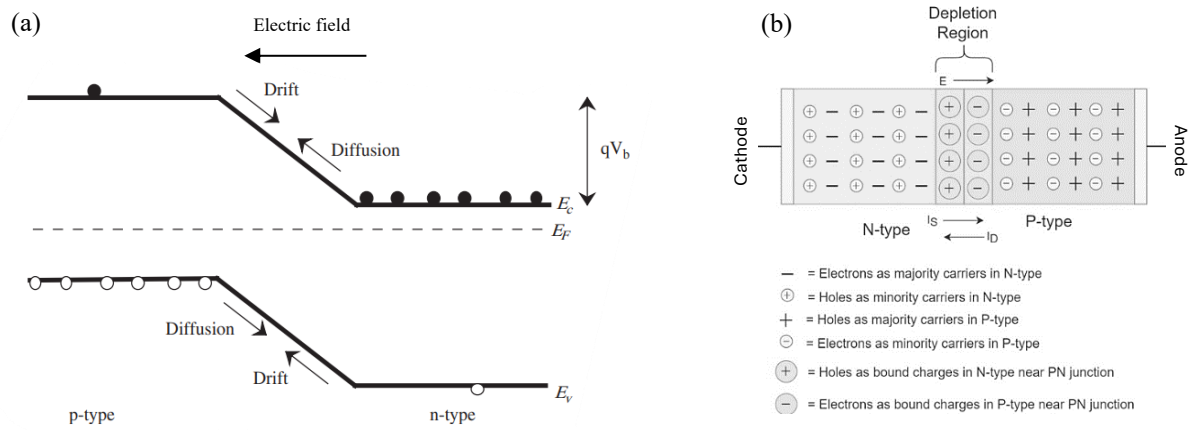

Figure 2. 2: *(a) Illustration of the band structure of a p-n junction. E_F is the Fermi energy level, E_C and E_V are the energy of conduction and valence band, respectively [38]. (b) Sketch of a p-n junction where I_S represents the direction of the drift current; I_D represents the direction of the diffusion current; E is the electric field generated in the SCR [40].*

When a p-n junction is exposed to light, photons with an energy greater than the energy bandgap are absorbed, generating electron-hole pairs. Electron-hole pairs are generated throughout the entire extent of the junction, but those produced within the n- or p-type material only partially contribute to the photocurrent. Indeed, if holes are generated in the n-type material, they recombine quickly because of the high concentration of electrons and the same happens to electrons generated in the p-type material. Instead, electrons-hole pairs generated within the

depletion region instantaneously feel the effect of the electric field that drives electrons toward the n-type material and holes toward the p-type material, reducing the probability of recombination. Hence, electron-hole pairs generated in the SCR will contribute at 100%, in an ideal case, to the electrical current generated.

2.3 Solar cell key performance indicators

To perform basic characterization of electronic devices, either a voltage is applied to measure a current, or current is injected and a voltage measured. In the case of p-n junctions, the current-voltage response is the following. When a forward bias (V_F) is applied on a semiconductor diode, with the positive terminal on the p-side and the negative terminal on the n-side, the applied voltage reduces the electrostatic potential across the depletion region [17,38]. In this case, the diffusion current is enhanced over the drift current: electrons are injected into the n-region and because of the smaller potential barrier, they cross the SCR with greater ease, thus feeding the minority carrier concentration in the p-region. Similarly, this happens to the holes injected in the p-region. At the contacts of the ideal diode the total current density is given by:

$$J = J_0\left(e^{qV_F/k_bT} - 1\right), \qquad \textit{Eq. 2.1}$$

where J_0 is the dark saturation current, k_b the Boltzmann constant, T the absolute temperature (K) and q the elementary charge. Instead, if a reverse bias voltage (V_R) is applied to the p–n junction, the applied voltage increases the electrostatic potential across the depletion region [17,38]. Therefore, the drift current dominates. Similarly, the current–voltage characteristics under reverse bias is given by:

$$J = J_0\left(e^{-qV_R/k_bT} - 1\right). \qquad \textit{Eq. 2.2}$$

Nevertheless, a real p–n junction does not follow an ideal current-voltage characteristic. In practical p–n junction solar cells, it is necessary to account for carrier recombination in the depletion region. Hence, the diode equation including the *ideality factor n* becomes:

$$J = J_0\left(e^{qV/nk_bT} - 1\right), \qquad \textit{Eq. 2.3}$$

where V is the applied bias, positive if it is forward and negative if it is backward. *Equation 2.3* allows to describe the current – voltage response of a p-n junction. In this model, band-to-band

recombination would correspond to $n = 1$ and defects-assisted recombination would lead to $n = 2$. A careful discussion about this topic is given in references [17,38].

When diodes are exposed to light, carriers are photogenerated in the SCR. They feel the electric field and start to drift in opposite directions. When the p- and n-sides are short-circuited the resulting current density, positive in direction of the holes, is termed as short-circuit current density (J_{SC}). For ideal diodes exposed to light, it equals the photogenerated current density (J_L), as can be derived from *Equation 2.4.*

$$J = J_0\left(e^{qV/nk_bT} - 1\right) - J_L. \qquad \textit{Eq. 2.4}$$

Instead, when an open circuit, between the p- and n-sides, is created, photogenerated carriers cannot be extracted and the voltage, at which therefore no-current flows, is called open-circuit voltage (V_{OC}). In both these conditions, no electrical power is produced.

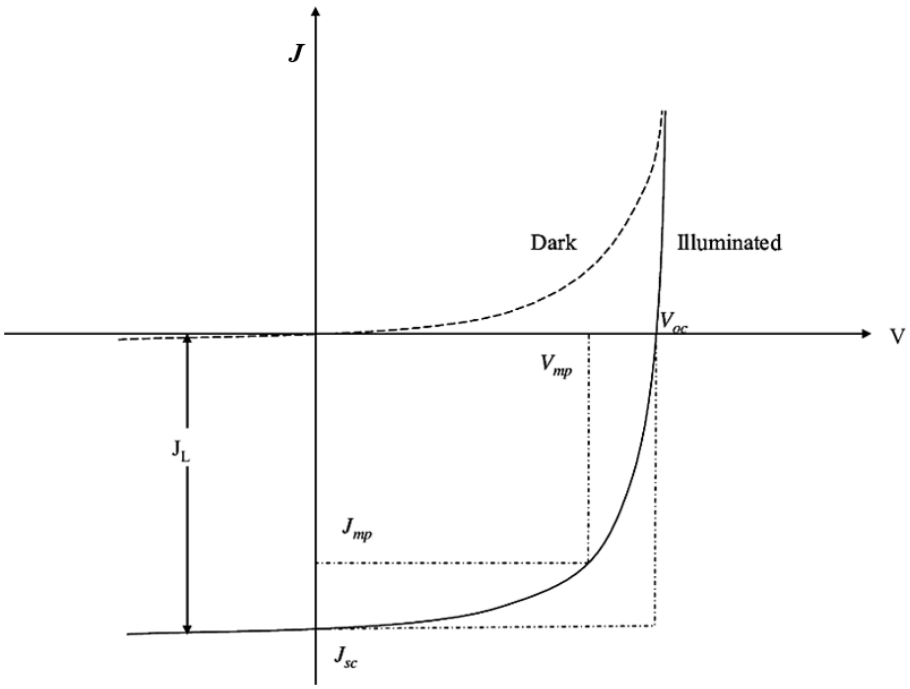

Figure 2. 3: *Example of ideal dark and illuminated current-voltage characteristics of a solar cell where V_{mp} and J_{mp} are the voltage and current density corresponding to the maximum power point on the I-V curve [41].*

As it can be seen *Figure 2.3,* the effect of the incoming light on the current density – voltage (JV) curve of an ideal diode in dark conditions is a negative translation along the *ordinate*. The intercept corresponds to the photogenerated current. Instead, the intercept of the curve with the *abscissa* represents the condition where no net-current flows due to the open-circuit condition.

Hence, the open-circuit voltage is obtained setting $J = 0$, leading to:

$$V_{\mathrm{OC}} = \frac{nk_{\mathrm{b}}T}{q} \ln\left(\frac{J_{\mathrm{SC}}}{J_0} + 1\right). \qquad \textit{Eq. 2.5}$$

The open-circuit voltage in a solar cell is the maximum voltage available from the cell when the net current through the solar cell is zero. It is a key parameter that indicates the potential difference between the positive and negative terminals of the cell under illumination. From *Equation 2.5* it is clear that V_{OC} depends on the short-circuit current density $\mathrm{J_{SC}}$ and on the ideality factor n. Moreover, it depends also on J_0. While J_{SC} typically has a small variation due to working conditions, the key parameter is the saturation current J_0, since this may vary by orders of magnitude [42]. The analytical expression for the saturation current is given in *Equation 2.6.*

$$J_0 = qn_{\mathrm{i}}^2 \left(\frac{1}{N_{\mathrm{A}}}\sqrt{\frac{D_{\mathrm{n}}}{\tau_{\mathrm{n}}}} + \frac{1}{N_{\mathrm{D}}}\sqrt{\frac{D_{\mathrm{p}}}{\tau_{\mathrm{p}}}}\right), \qquad \textit{Eq. 2.6}$$

where n_i is the intrinsic carrier concentration, N_{A} and N_{D} are the acceptor and donor concentrations, respectively, D_{n} and $\mathrm{D_p}$ are the diffusion coefficients for electrons and holes respectively and, τ_{n} and τ_{p} are the lifetimes for electrons and holes, respectively.

From *Equation 2.6* it is evident that the open-circuit voltage is also a measure of the recombination in the device. If a high recombination rate is considered, the carrier lifetimes are reduced. Therefore, $\mathrm{J_0}$ increases, lowering the value of $\mathrm{V_{OC}}$. In the case of a low recombination rate, $\mathrm{V_{OC}}$ increases. Hence, $\mathrm{V_{OC}}$ is inversely related to the rate of recombination within the solar cell. Minimizing recombination is crucial for maximizing the open-circuit voltage and, consequently, the overall efficiency of the solar cells.

Another parameter of a solar cell is the fill factor (FF), it is obtained dividing the maximum power density by the product of $\mathrm{V_{OC}}$ and $\mathrm{J_{SC}}$ as in *Equation 2.7,* where $\mathrm{V_{mp}}$ and $\mathrm{J_{mp}}$ are the voltage and current density corresponding to the maximum power point on the I-V curve.

$$FF = \frac{J_{\mathrm{mp}}V_{\mathrm{mp}}}{J_{\mathrm{SC}}V_{\mathrm{OC}}}. \qquad \textit{Eq. 2.7}$$

The fill factor is a key parameter in evaluating the performances of solar cells. The higher the fill factor, the lower the losses within the cells due to resistances [38]. Moreover, graphically the FF defines the *squareness* of the JV curve.

Finally, the conversion efficiency (η) of the solar cell is defined as the ratio of the generated maximum electric output power density to the total power density coming from the incident light (P_{in}) [38].

$$\eta = \frac{J_{\mathrm{mp}} V_{\mathrm{mp}}}{P_{\mathrm{in}}} = \frac{J_{\mathrm{SC}} V_{\mathrm{OC}} FF}{P_{\mathrm{in}}}. \qquad \textit{Eq. 2.8}$$

To maximize the efficiency, it is necessary to improve all the other three photovoltaic key performances indicators (KPI): V_{OC}, J_{SC} and FF.

Although the study of ideal models can be useful to understand the basic working processes of solar cells, real diodes generally contain parasitic resistances that decrease their efficiency through power dissipation. These resistances include series (R_S) and shunt (R_{SH}) resistances. The main contribution to series resistance comes from the bulk resistance of the semiconductor material and the contact resistance between the semiconductor material and metallic resistance of the electrodes [14,43]. In instances of very high R_S , the short-circuit current density degrades. However, R_S does not influence the open-circuit voltage, as no current flows through the solar cell at V_{OC}. On the other hand, shunt resistance R_{SH} is mainly affected by fabrication defects and crystal defects or impurities located in the depletion zone, which reduce the R_{SH} [14,44]. It offers an alternative path for the light-generated current, thereby increasing the current flowing through the solar cell.

When both series and shunt parasitic resistances are present in a solar cell, the J-V curve is described by the following equation:

$$J = J_{\mathrm{L}} - J_0 \left(e^{\frac{q(V + JR_{\mathrm{S}}A)}{nk_{\mathrm{b}}T}} - 1 \right) - \frac{V + JR_{\mathrm{S}}A}{R_{\mathrm{SH}}}, \qquad \textit{Eq. 2.9}$$

whit *A* being the photoactive area of the solar cell.

2.4 Unintentional doping concentration

In *Figure 2.2*, the electric field across the SCR was introduced as the driving force for carrier separation in p-n junction solar cells. For absorber materials with short minority carrier lifetimes and diffusion lengths, embedding them as intrinsic material in a *p-i-n* junction can improve carrier collection. In this case, the SCR extends across the whole *i*-layer and carriers are collected through a field assisted drift process [45].

However, the field assistance diminishes if the absorber is unintentionally doped and loses its intrinsic nature. Unintentional doping (UID) can originate from impurities incorporated during crystal growth (carbon atoms, for example, act as acceptors in GaAs) or from defects in the material (like nitrogen related point defects in InGaAsSbN) [46].

Figure 2.4 illustrates the effect of how p-type UID in the i-layer alters the potential across a p-i-n junction.

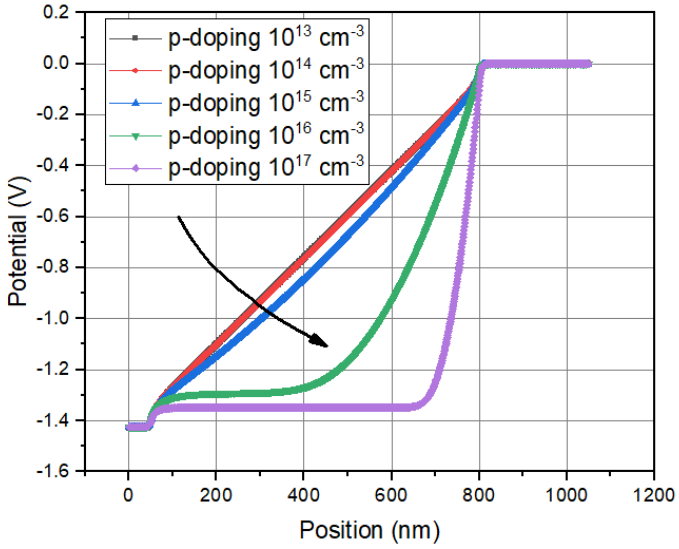

Figure 2. 4*: Simulation of how potential across a p-i-n junction is lost for UID (p-type) above 10^{16} cm^{-3} [47]. The position (nm)indicates the spatial coordinate across the p-i-n junction where the potential is evaluated.*

For a p-type doping of 10^{16} cm^{-3} or above, a region of flat potential in the intrinsic layer forms at the p-i interface and a p-n junction forms at the i-n interface. In the region of flat potential, the electric field vanishes and field assistance for carrier collection is lost.

Therefore, UID can significantly reduce carrier extraction and J_{SC} and it has an important detrimental effect in solar cell performance.

To assess the presence of UID, capacitance-voltage (CV) profiling can be performed. In CV profiling, the SCR is approximated as a parallel plate capacitor of capacitance

$$C = \frac{\varepsilon A}{w} \qquad \textit{Eq. 2.10}$$

where ε and A are the dielectric constant of semiconductor and the surface area of the diode, respectively. The depletion width w depends on the applied bias through

$$w = \sqrt{\frac{2\varepsilon}{q}\left(\frac{1}{N_A}+\frac{1}{N_D}\right)(V_{bi}-V)}\,, \qquad \textit{Eq. 2.11}$$

where V is the applied bias, q is the electron's charge, N_A and N_D are the acceptor and donor concentrations respectively. Assuming an asymmetric doping ($N_A < N_D$) results in an UID-concentration ($N_{UID} \sim N_A$) that can be derived from a voltage dependent measurement of the device capacitance:

$$N_{UID} = \frac{2}{q\varepsilon A^2}\left(\frac{d(1/C^2)}{dV}\right)^{-1}. \qquad \textit{Eq. 2.12}$$

The relation between N_{UID} and w is referred to as an *apparent doping profile*.

Figure 2.5 shows the simulated apparent doping profile for the p-i-n junction with doping of 10^{16} cm^{-3} from *Figure 2.4*. It illustrates how to interpret CV results. At high negative bias voltages (region 1), the UID layer is completely depleted of mobile carriers and doping in the p and n layers is detected. Under positive bias (region 2), the junction becomes conductive and apparent doping profile no longer reflects the actual concentration within the i-layer. A reliable determination of the UID in the i-layer is only possible for a small voltage range in between region 1 and 2.

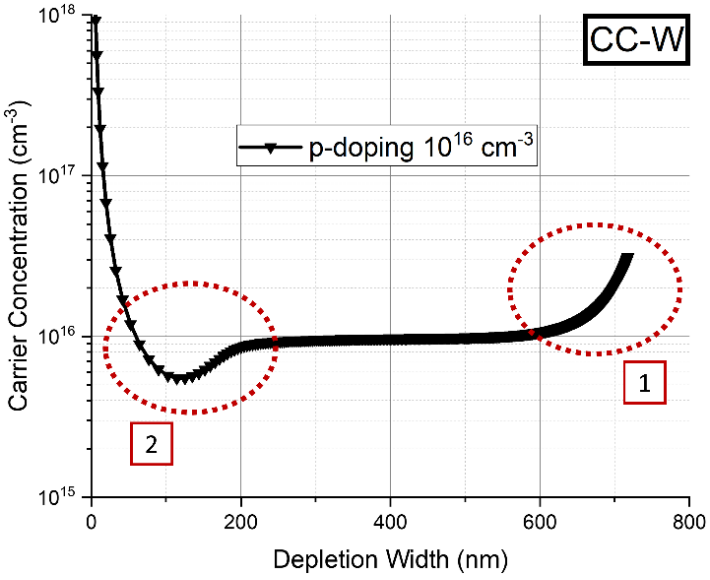

Figure 2. 5*: Simulated apparent doping profile for a p-i-n junction UID (p-type) of 10^{16} cm^{-3}. The carrier concentration can only be determined reliably between the highlighted regions 1 and 2 [47].*

The devices studied in this work have a p-i-n structure and are analysed regarding UID with the described method.

3. Quantum dot solar cells

The technological development of solar cells focuses on increasing energy conversion efficiency. One of the emerging technologies with the potential to achieve this goal are quantum dots solar cells. Before delving into the working principle of QDSCs, the fundamental physics of QDs is introduced.

3.1 Physics of quantum dots

In a bulk semiconductor, excited electrons and holes have a continuously high density of state (DOS), therefore they can move freely in the conduction and valence band, respectively. However, if carriers are confined in one or more directions, the DOS changes and the continuous parabolic dependence of DOS on energy for bulk materials reduces to several discrete levels for a quantum box, as depicted in *Figure 3.1*.

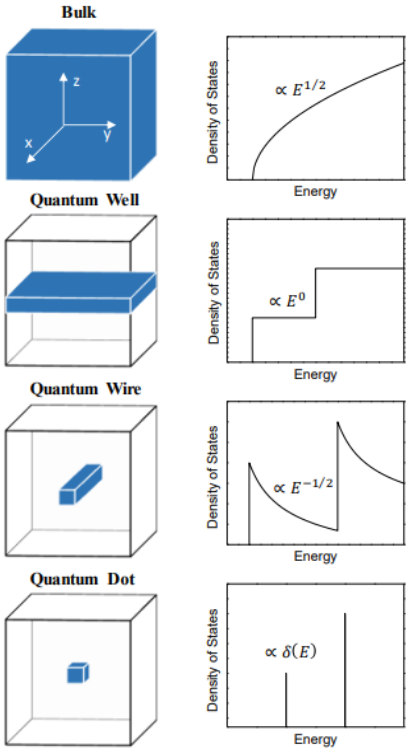

Figure 3. 1: *The four different cases of quantum confinement (left), with the corresponding density of states as a function of the energy (right) [30].*

In quantum dots, the area where the electrons can move freely is termed "*potential well"*, which is created when the QD is embedded within the barrier material. Conversely, the area where motion is restricted is known as a "*potential barrier*" as shown in *Figure 3.2*. Therefore, a useful approximation of electron-hole pairs behaviour in QDs is likened to a particle confined within an infinite potential well, conceptualizing the QD as a quantum box [48-49].

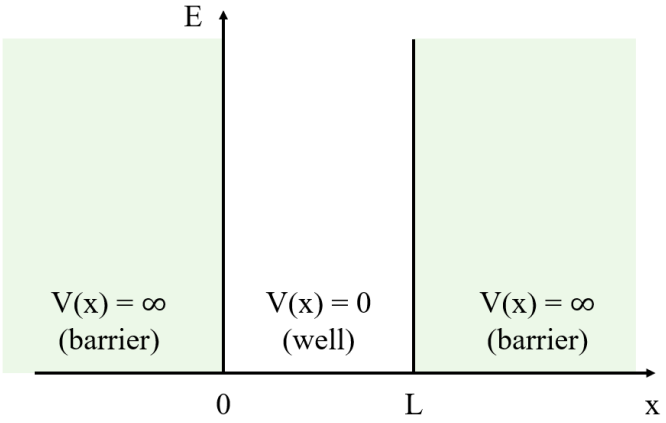

Figure 3. 2: *1 dimensional quantum Box Model scheme. The particles can move freely in the well region and cannot overcome the infinite potential barriers at the edge.*

The energy levels of quantum confinement, in the case of a QD (cubic box), can be calculated using the following equation:

$$E_n = \frac{n^2 h^2}{8\mu L^2} \qquad \textit{Eq. 3.1}$$

where h is the Plank's constant, n is a positive integer, μ is the effective mass of electrons and holes, used to account for the interaction with the periodic potential of the crystal lattice, and L is the dimension in which electrons are confined [49].

Conventionally, there is a spherical confinement of electron-hole pairs in QDs rather than a square [49]. Therefore, it is possible to interchange the length L with radius R. The energy eigen-state solution for electron-hole pairs (exciton kinetic energy) becomes:

$$E_n = \frac{n^2 h^2}{8\mu R^2} \qquad \textit{Eq. 3.2}$$

The electron-hole pairs are not confined in an empty space but rather inside a host semiconductor crystal (material of which the QD is made), thus the semiconductor fundamental

band gap energy becomes the baseline energy of the system [49]. Hence, the minimum energy needed to excite charge carriers in the QDs is made up of two main energy contributions (for small R limit). The first energy contribution is the infinite crystal band gap of the host semiconductor, which is the characteristics of the material; the other crucial contribution is the exciton kinetic energy, which represents the potential well contribution due to quantum confinement of exciton, as shown below [49]:

$$E_{g(QDs)} = E_{g(bulk)} + \frac{n^2h^2}{8\mu R^2}. \qquad \textit{Eq. 3.3}$$

If it is not possible to assume the small R limit, in the previous equation it must also appear a term which represents the electrostatic energy contribution due to Coulomb's attraction between the electron and the hole [49].

From *Equation 3.3* it is clear how the QD ground state transition increases with a decrease in size of the quantum dot. Accordingly, as the size of the QD decreases, a blue shift in the absorption peak of the QD is observed, as depicted in *Figure 3.3* [50].

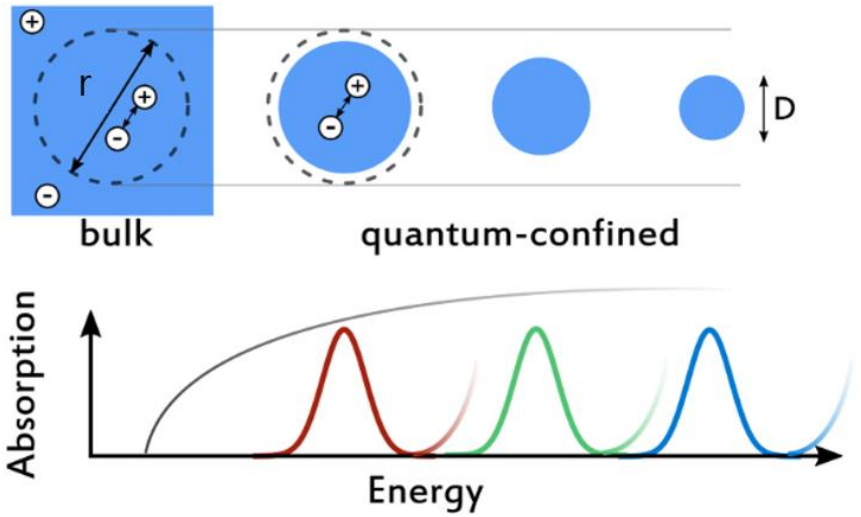

Figure 3. 3: *Qualitative trend in the absorption peak of QDs with different size [50].*

Quantum dots can be fabricated by several methods such as colloidal chemistry, lithography and epitaxial growth [51-52]. In this thesis, only self-assembled epitaxial growth of QDs will be presented.

3.2 Self-assembled epitaxial growth of quantum dots

For semiconductor materials the most common way to grow QDs is a self-assembling process using molecular beam epitaxy (MBE). MBE is used to obtain thin-film deposition of single crystals [53-54]. In solid source MBE, elements such as gallium and arsenic, in ultra-pure form, are heated in order to promote the reaction in gas phase of one or more thermal molecular beams with a crystalline surface [55].

The fundamental understanding of the thin-film growth process, growing QDs by MBE, is analogous to the theory of liquids spreading over a surface. The balance between cohesive forces within the film and adhesive forces between the film and substrate atoms determines the contact angle and, ultimately, whether the film will adhere to the substrate. In 1958, Ernst Bauer categorized the growth of epitaxial films into three distinct modes, as depicted in *Figure 3.4* [30,56-57-58].

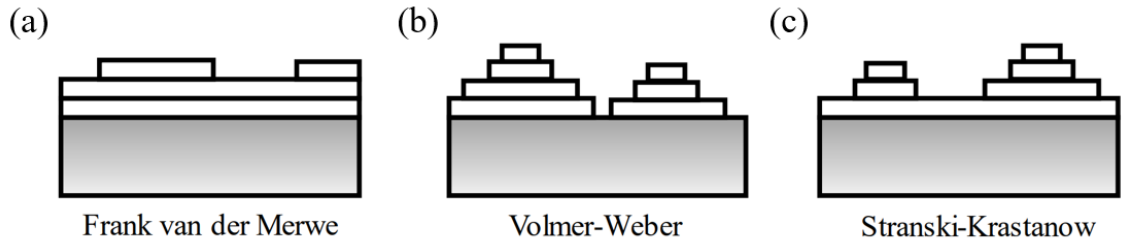

Figure 3. 4: *Basic growth mechanisms: (a) Frank-van der Merwe mechanism (layer-by-layer growth), (b) Volmer–Weber mechanism (island growth), (c) Stranski-Krastanov mechanism (layer-plus-island growth) [30].*

In the *Frank-van der Merwe* mode, the growth involves the coalescence of monolayer (ML) height islands before nucleation of a new layer atop them. Conversely, in the *Volmer-Weber* mode, the growth proceeds to many atomic layers forming discrete islands before merging [30-57].

The *Stranski-Krastanov* (SK) mode initiates in a layer-by-layer manner, with island formation after reaching a certain layer thickness. This growth mode is common if there is lattice mismatch between the grown layer and the substrate material [30,57]. Hence, the SK-mode relies on lattice mismatch between the substrate and the grown layer. Lattice mismatch refers to the difference in lattice parameters between two materials. In *Figure 3.5* the lattice constants for some semiconductors, with their corresponding bandgap energy, are illustrated.

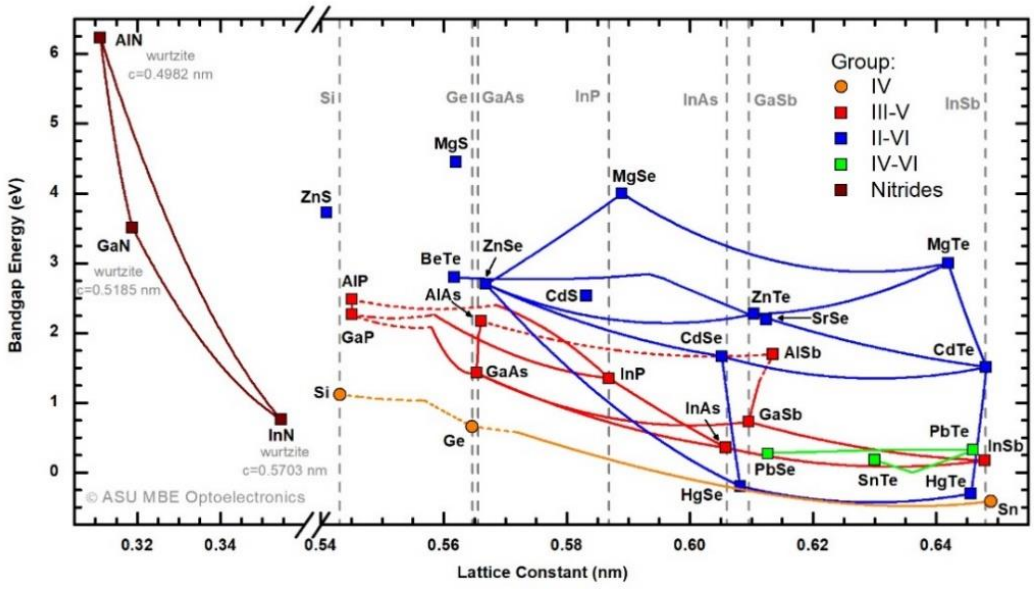

Figure 3. 5: *Energy bandgap as function of the lattice constant for typical semiconductors [59].*

When heterostructures are grown, the lattice constants either match (AlP/GaP), or they do not match (InAs/GaAs). In the latter case, deformation occurs as the epitaxial layer adjusts to match the lattice of the substrate, generating elastic energy primarily in the lattice of the grown layer. When this energy surpasses a critical value, it can be alleviated in two ways [57]. One method involves nucleating nanosized islands, known as quantum dots, on the surface of the even layer, allowing lateral relaxation of atomic planes and reducing elastic energy. Alternatively, misfit dislocations can be generated at the interface [57]. A schematic of the Stranski-Krastanov grow is shown in *Figure 3.6*.

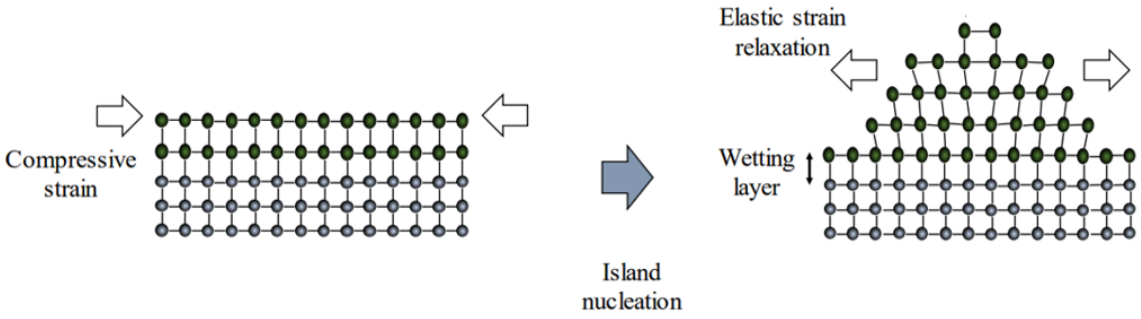

Figure 3. 6: *Stranski-Krastanov island formation during the epitaxial growth. Initially, the epilayer grows layer-by-layer (top) until it reaches a critical thickness. Then, compressive strain elastically relaxes giving rise to the more energetically favourable three-dimensional growth (bottom). Taken from [30].*

The following section introduces GaAs/InAs QDs growth, that is the material system studied in this thesis.

3.3 InAs/GaAs quantum dots

InAs self-assembled QDs grown in the Stranski–Krastanov growth mode have been intensively investigated for optoelectronic device applications [60-61-62]. The InAs/GaAs heteroepitaxial system has a lattice mismatch of ~7% and QDs are typically grown in the Stranski–Krastanov mode, on a (001) GaAs surface, after the growth of ~ 1.6 – 1.8 monolayers [30,63-64]. Once capped with GaAs, InAs/GaAs QDs form a double heterostructure (DHS) of GaAs/InAs/GaAs leading to the confinement of both electrons and holes within the islands [30,64]. Various parameters, such as the effects of growth rate, growth temperature, amount of deposited InAs quantum dot and capping layer materials influence the growth [30,65-66]. By carefully adjusting these growth conditions, size, shape and density of surface QDs can be tailored, ultimately influencing their optical and electronic properties. However, these QDs are strongly altered during the capping process, which limits the tunability.

Before capping, SK-growth can lead to QD-heights between 4-10 nm. Nevertheless, after capping with GaAs, the now buried QDs are typically 3-4 nm high [66-67]. It is commonly accepted that In-Ga intermixing at the interface is driving the dissolution process that leads to the height reduction [27,57]. The dissolution of quantum dots during the capping process is often attributed to the introduction of additional strain, which is mitigated through In-Ga intermixing. In *Figure 3.7* the average height of InAs/GaAs QDs, before and after capping with GaAs, is depicted.

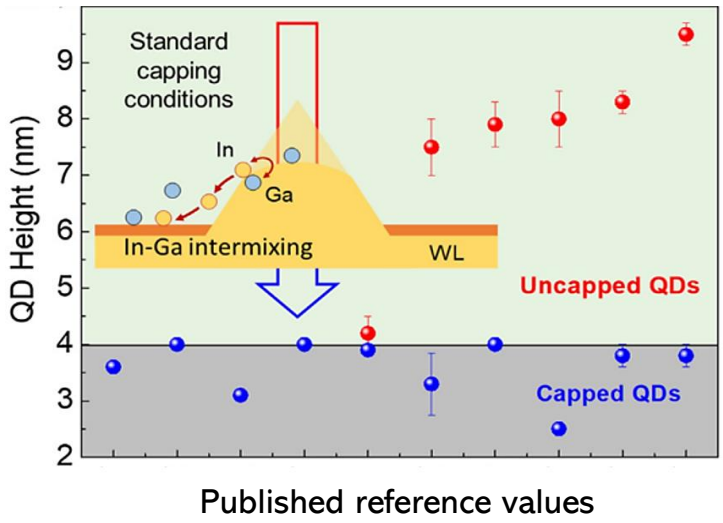

Figure 3. 7: *The average height of InAs/GaAs QDs before and after the capping process is shown by the red and blue dots, respectively. The data have been published by different authors. The inset illustrates a schematic of the QD dissolution process during capping, where the top of the QD flattens due to surface In-Ga intermixing, and surface diffusion of In leads to the thickening of the wetting layer [30][67].*

Although this effect may initially be seen as a drawback, it represents a potential advantage, as it allows for the modification of optoelectronic properties solely by altering the growth conditions of the capping layer, and its nature [67-68-69]. The effect of the CL on the size of the QDs was studied by D. Gonzalez *et al*. [70].

3.4 Strain-reducing capping layers: type-I to type-II transition

Since GaSb has lattice parameter closer to that of InAs than GaAs (*Figure 3.5*), the use of a GaAsSb capping layer minimizes the strain between the QDs and the overgrown layer. In a work by J.M. Ulloa *et al.* [71], it has been calculated that using a $GaAs_{0.75}Sb_{0.25}$ capping layer results in 28% less strain in InAs QDs compared to using a GaAs CL.

The strain reduction counteracts the dissolution of the QDs during overgrowth [14,30,72-73]. As depicted in *Figure3.8*, the higher the Sb content, the better the dissolution is prevented. In this way the QD height is preserved, and the transition energy gap is red shifted (*Equation 3.3*).

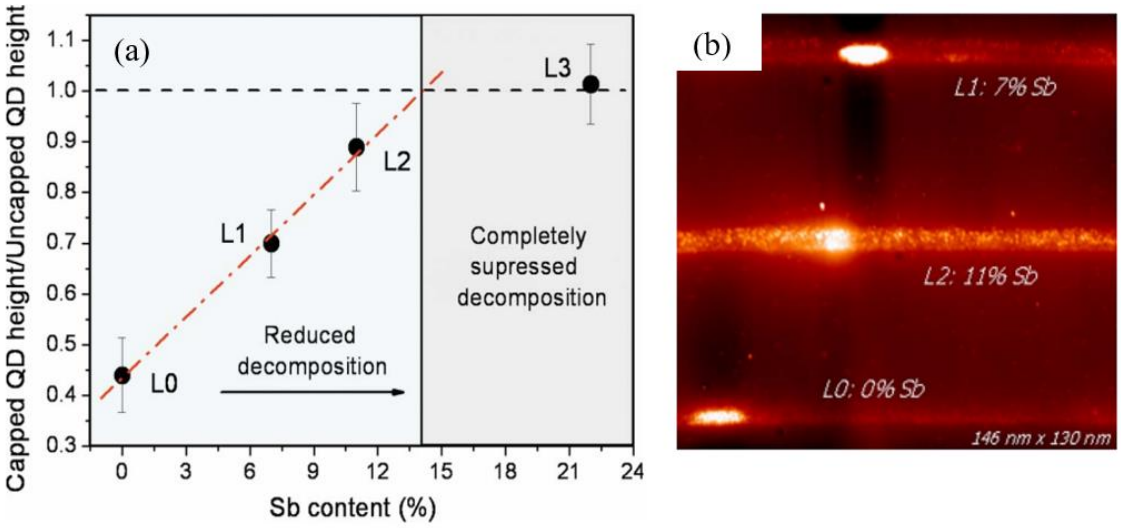

Figure 3. 8: *(a) QD height normalized to the height of the equivalent uncapped QDs as a function of Sb content in the four different layers studied by cross-sectional scanning tunnelling microscopy (X-STM). A value of 1.0 indicates complete suppression of the decomposition process. The red line represents a linear fit to the values of L0, L1, and L2, the three levels distinguishable from the STM image. (b) Topography-STM images of QDs with different Sb content in the CL, 0%, 7% and 11%. Taken from [62].*

Furthermore, the presence of the CL leads to a modification in the electronic structure of the barrier material [74]. The addition of Sb predominantly affects the valence band of GaAs

[62,73]. With increasing Sb content, the GaAs valence band progressively shifts to higher energies, modifying the ground state energy of the holes in the QD. For high Sb content (> 14-16%) the ground state is found in the capping layer and not in the QD anymore. This effect is referred to as "*type-I to type-II transition*" in the band alignment in the heterostructures [62,73]. An illustration of the valence band modification as the Sb content increases is depicted in *Figure 3.9.* As it can be noticed, the localization of the holes in the CL also affects the energy band gap of the nanostructure, which is red shifted to lower energies.

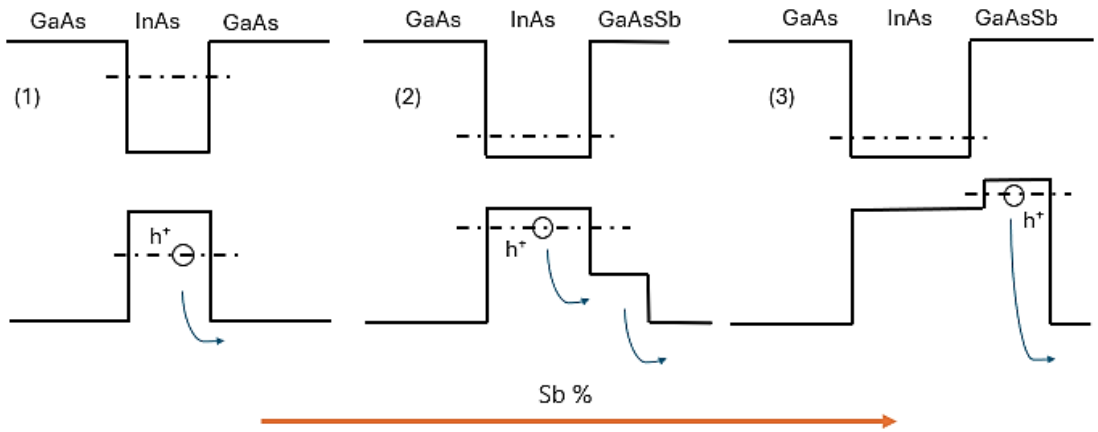

Figure 3. 9: *Illustration of the band structure and carrier escape mechanism from the nanostructure for systems with different CLs. (1) represents the case with 0% of Sb. (2) represents a type-I systems with GaAsSb CL. (3) represents a type-II systems with GaAsSb CL.*

The type-I to type-II transition strongly affects the optoelectronic properties of the QDs for the following two reasons.

Firstly, the confinement of the holes in the capping layer leads to a reduced electron-hole wavefunctions overlapping. For Sb contents exceeding the 14 – 16% threshold, the hole wavefunction moves from the base of the QD to the capping layer. On the other hand, electrons remain confined in the QD. Hence, the spatial separation of the electron-hole ground states reduces wavefunctions overlapping. This effect leads to an increased radiative lifetime [30,73].

The transition from type-I to type-II also influences the extraction of carriers from the nanostructure, as studied in [73,75-76]. Considering the different band alignments depicted in *Figure 3.9*, three possible hole escape mechanisms can be identified: holes escape from the QD to the GaAs barrier material (1), holes escape from the QD to the GaAs barrier material through

a two-steps process that involves the GaAsSb CL (2), and holes escape from the GaAsSb capping layer to the GaAs barrier material (3) [73].

Ulloa *et al.* in [73] demonstrated that the calculated barrier energy for holes in the ground state slightly decreases as the Sb content increases. Consequently, the barrier energy for holes to be excited to the valence band of the GaAsSb CL (escape mechanism (2)) decreases for Sb contents up to 16% [73]. This energy eventually reaches zero at 14 – 16% Sb when transitioning into the type-II alignment. Now, the lowest energy state for the holes is situated outside of the QD in the GaAsSb capping layer (*Figure 3.9(3)*). In this scenario, holes must escape directly to the GaAs valence band (escape mechanism (3)), with a significantly higher barrier. This barrier further increases for higher Sb contents.

Although type-II capping layer structures have advantages mainly linked to their longer radiative lifetime, they also face growth challenges. While systems with a low content of Sb in the CL present flat growth fronts in all the stacked QD layers, increasing the concentration of Sb leads to a progressive bending of the layers where QDs were deposited from the bottom to the top [77]. This effect is shown in the dark-field cross-sectional TEM images in *Figure 3.10(c),* from [77].

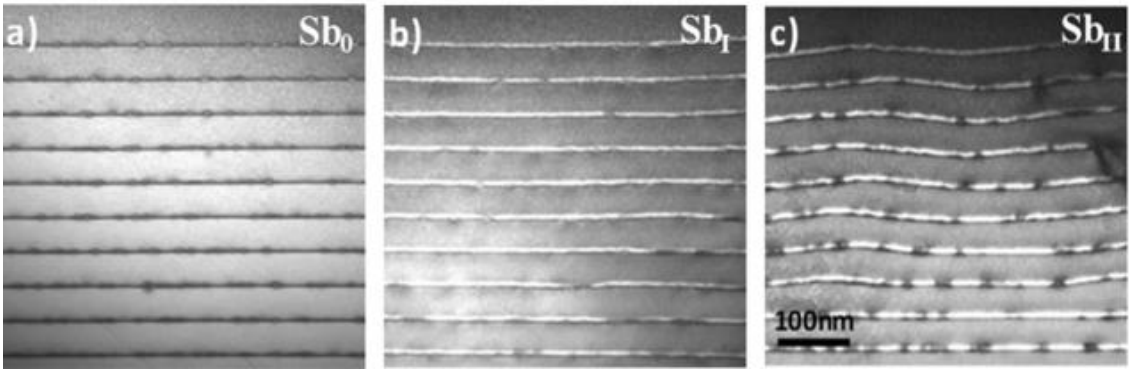

Figure 3. 10: *Dark-field cross-sectional TEM images for three different samples. a) no Sb in the CL. b) 10% of Sb in the CL. c) 22% of Sb in the CL. Increasing the Sb contend extended defects appear in the structures [77].*

Although GaAsSb CLs reduce strain inside QDs, the overall strain in the structure increases, since a material with a larger lattice parameter than GaAs is added. Due to the strong accumulated compressive strain, in the high Sb content type-II structures, extended defects are generated. They are a critical source of non-radiative recombination [30,78-79]. The following section treats how InAs QD and GaAsSb capping layer systems are beneficial in terms of an application in solar cells.

3.5 Advantages and drawbacks of QDSCs

As explained in Section 1.4, the idea of using InAs QDs in solar cells is to extend the absorption range of GaAs SJSCs or MJSCs. In the case of MJSCs, this would increase the photogenerated current in the GaAs sub-cell for current matching.

By embedding QDs in the intrinsic region of a p-i-n junction, the band structure of the obtained QDSCs is complemented by the discrete energy levels of the nanostructures. An illustration of the band structure of a GaAs/InAs QDSC is shown in *Figure 3.11*.

The difference between the ground and excited states of InAs quantum dots is smaller than the energy difference between VB and CB of GaAs. In this way photons below the GaAs energy gap can be absorbed. This extends the absorption range of the cell into the infrared region of the solar spectrum, thereby enhancing cell efficiency [80].

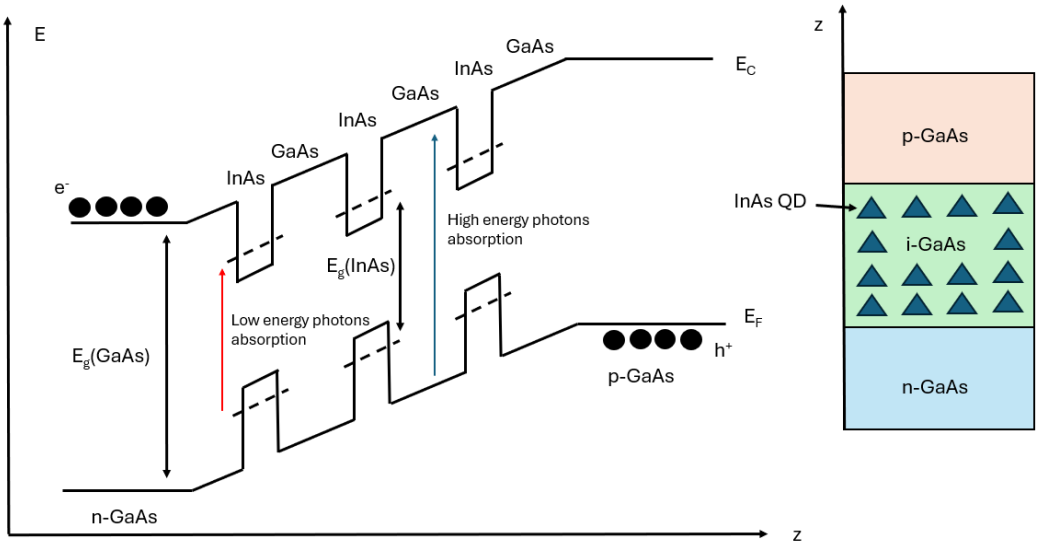

Figure 3. 11: *Band structure for a InAs/GaAs QDSC. (left) photons of lower energy (between the levels) are absorbed by InAs. Photons with high energy are absorbed by GaAs between CB and VB. (right) A schematic for a p-i-n junction with embedded QDSC.*

Although incorporating quantum dots into the host material broadens absorption ranges, it also comes with drawbacks [30]. Firstly, the strong carrier localization and efficient radiative recombination within the QDs contribute to voltage losses. Furthermore, the small absorption volume of QDs leads to a relatively minor contribution to light absorption, necessitating the stacking of multiple QD layers to increase their overall contribution to the total cell current. However, this stacking practice generates strain accumulation in the overall structure, which can promote the formation of extended defects [30,78-79]. These defects are a critical source

of non-radiative recombination thereby limiting the maximum number of QD layers that can be integrated into the devices. [30,78-79].

The use of GaAsSb capping layers is a promising approach to address these challenges [81-82].

As described in Section 3.4, the GaAsSb capping layer red shifts the ground state transition and thereby increases the absorption range of the InAs QDs. In Type-I structures, this enhancement extends the wavelength of absorbed photons up to 1400 nm, while type-II structures extend absorption beyond 1500 nm [77].

Further the capping layer eases carrier extraction through increased radiative lifetime. In the case of type-I systems, carrier extraction is further improved by relaying on a two steps process (Section 3.4). Despite even longer lifetime for type-II systems, here the increased potential barrier could hinder extraction. In light of this, choosing the system that best utilizes the advantages associated with each band alignment, is essential.

4. Experimental techniques and methods

In this thesis, QDSCs of p-i-n structure solar cells, grown and processed by A. Utrilla *et al.* [30] are further analysed as a function of temperature and by taking into consideration unintentional doping. This chapter describes the samples, the characterization techniques and the setups employed.

4.1 Description of the samples

Four different QDSCs with the structure depicted in *Figure 4.1* are studied. The QD layers were grown in 10 equally spaced layers in the i-GaAs layer of a p-i-n junction by A. Utrilla *et al.* [30]. Each InAs QD layer is covered by a 20 ML-thick $GaAs_{1-x}Sb_x$ CL with nominal Sb contents of 0, 5, 17 and 22% (samples referred to as S-Sb_0, S-Sb_5, S-Sb_17 and S-Sb_22). A 10 ML-thick GaAs layer (LT-layer) was grown immediately after the CL. The QD layers are sandwiched in the middle of a 400 nm-thick intrinsic GaAs layer, grown on a 500 nm-thick n-GaAs base buffer and ended with a 350/150 nm-thick p-/p+ -GaAs layer. Mesa-eatched solar cell devices with 200 μm diameter were finally processed and mounted on a transistor outline through wire bonding following the procedure described in [30]. The structure of these cells is not optimized. No window layer or back surface field layer have been used at this point. Nevertheless, these samples serve for comparative purposes.

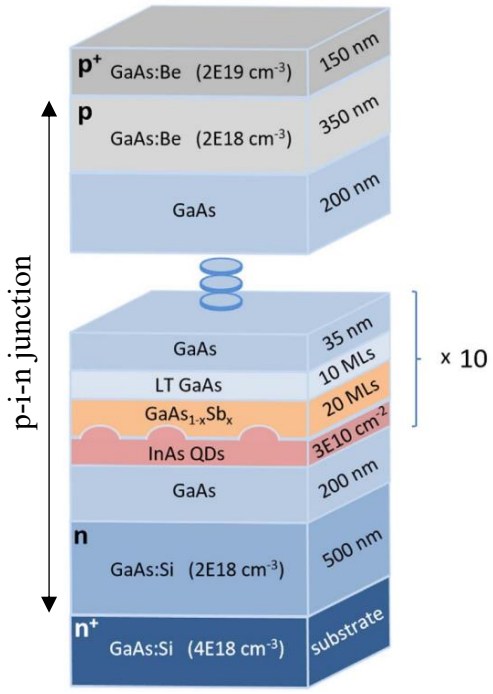

Figure 4. 1: *Sketch of the p-i-n junction structure used in this work. 500 nm of Si-doped-GaAs were epitaxially grown on a n^+-GaAs substrate. Then, 200 nm-thick intrinsic GaAs layer was deposit. Ten layers of nanostructured materials have been deposited, consisting in complex alternated structure made by a high density InAs QDs layer, 20 MLs-thick of $GaAs_{1-x}Sb_x$ CLs, 10 MLs-thick undoped GaAs layer grown at low temperature (LT) and 35 nm-thick of undoped GaAs layer grown at high temperature (HT). Once obtained ten of these structures a further layer of i-GaAs was deposited with a thickness of 200nm. Finally, 350 nm-thick of p-GaAs and 150 nm-thick of p^+-GaAs (both doped with Be) covered the whole structure [30].*

An example of the sample mounted on the transistor outline is shown in *Figure 4.2 (a)*. In this particular case TO-8 was used as transistor outline. It is a type of electronic package used for housing semiconductor devices, particularly transistors, diodes, and integrated circuits. The TO-8 package leads connect the internal semiconductor device to an external circuit. In *Figure 4.2 (b)* a magnification of one of the diodes is shown.

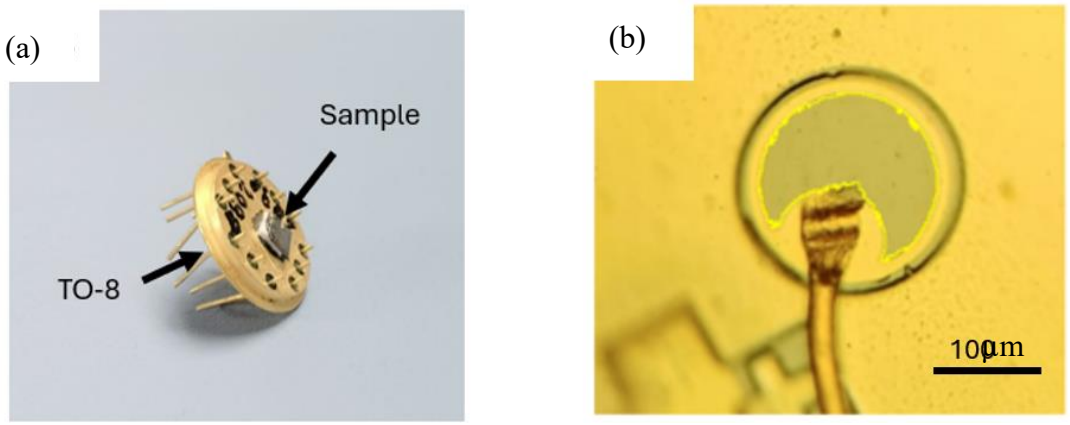

Figure 4. 2: *(a) Sample bonded on the TO-8 holder. (b) Image acquired with the optical microscope (Laica Leitz DMRX (Laica, Germany)) for one of the diodes measured. The photoactive area is the half grey moon (right).*

4.2 Solar spectrum

The solar spectrum ranges from 250 to 3000 nm [83]. The amount of solar irradiation reaching the Earth's surface is dependent on the path length through the atmosphere, which is dictated by the angle of the sun relative to the normal to the Earth's surface at a specific location. The length of the path is quantified by a coefficient known as air mass (AM), which is equal to 1 for normal incidence [84]. For energy conversion purposes, it is useful to standardize the operation of devices and processes to a reference spectrum (*Figure 4.3(a)*) [84-30]. Two commonly used reference spectra are AM0, corresponding to solar radiation outside the atmosphere, and Air Mass 1.5 (AM1.5), describing radiation reaching the Earth's surface after passing through 1.5 times a standard air mass, with the sun at 48.19° [82-30]. An illustration is given in *Figure 4.3(b)*. The AM0 spectrum is defined by the international standard ASTM E-490 of the American Society for Testing and Materials [85], representing typical spectral solar irradiance outside of the atmosphere ($\Phi_E^{AM0} = 1366.1\ W\ m^{-2}$). For terrestrial irradiance under an absolute air mass of 1.5, two reference spectra are defined. One of them is the AM1.5-Global (ASTM G173) [86], with solar irradiance of:

$$\Phi_{\mathrm{E}}^{\mathrm{AM1.5G}} = 1000.4\ \mathrm{W\,m^{-2}} = 100.04\ \mathrm{mW\,cm^{-2}}.$$

The other reference spectrum for terrestrial irradiance is AM1.5-Direct (ASTM G173). It is defined for applications of solar concentrators and has an integrated power density of 900.1 W m^{-2} [86]. The ASTM AM1.5G terrestrial solar spectrum represents the standard accepted by the international community for evaluating materials [30]. In *Figure 4.3 (a)* the three different spectra are shown. It can be seen how the spectra differ in intensity due to selective absorption by low concentration gases. This leads to significant decreases or complete extinction of radiation in specific wavelength ranges, as depicted in *Figure 4.3(a)*. In this work, solar cells have been studied under AM1.5G conditions.

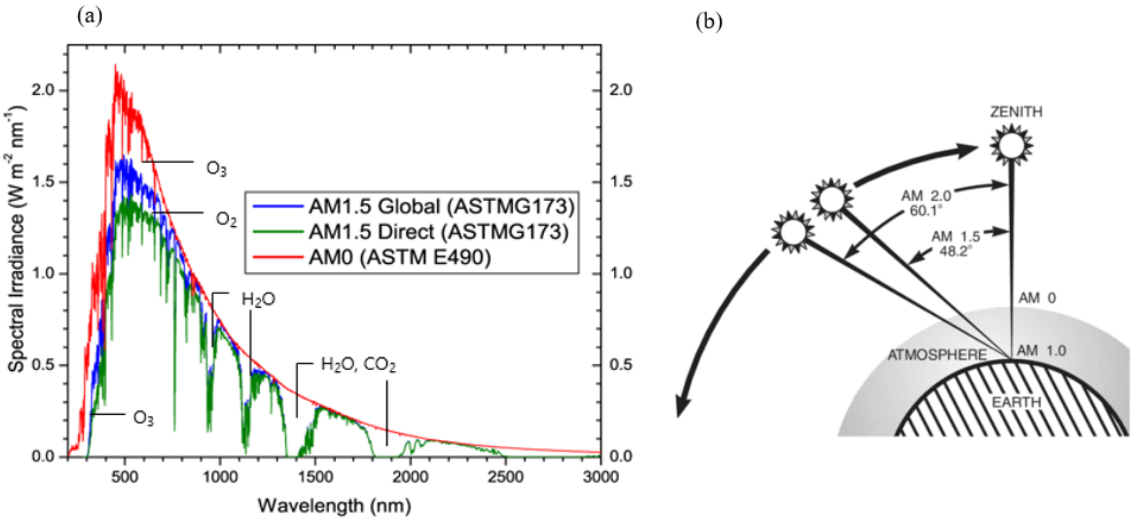

Figure 4. 3: *(a) Spectral radiance for the three different standards, including the influence of some of common atmospheric gases. (b) Conceptual view of AM0, AM1 AM1.5 and AM2 [87][88].*

4.3 Optoelectronic setups

The devices mounted on TO-8 are characterized in the different experimental setups described below. The different characterizations were performed over several diodes for each sample.

4.3.1 Current – voltage and capacitance – voltage measurements setup

In this thesis JV curves under different illuminated and temperature conditions are analysed. A schematic of the setup used to carry out these measurements is shown in *Figure 4.4*.

JV curves under dark conditions

First, this optoelectronic configuration enables JV measurement in darkness as a function of temperature. For this purpose, a cryostat system, cooled down using closed cycle liquid He in high vacuum conditions, is used. Therefore, the samples, mounted on a TO-8 holder are placed in a vacuum chamber connected to a compact turbo rotary pump, HiCUBE (PFEIFFER VACUUM, Germany) to create a pressure as low as 3.4 x 10^{-5} mbar. The chamber is connected to an Oxford Cryodrive 1.5 (Edwards High Vacuum Int., Israel) and an Oxford ITC502 PID Intelligent Temperature Controller (OXFORD Instrument, England). The combination of Cryodrive 1.5 and ITC502 PID allows for precise measurements over a wide temperature range.

For these measurements the voltage is applied and controlled using a K230 Keithley (Keithley, Ohio) voltage source and the current is measured with a K617 Keithley (Keithley, Ohio) electrometer.

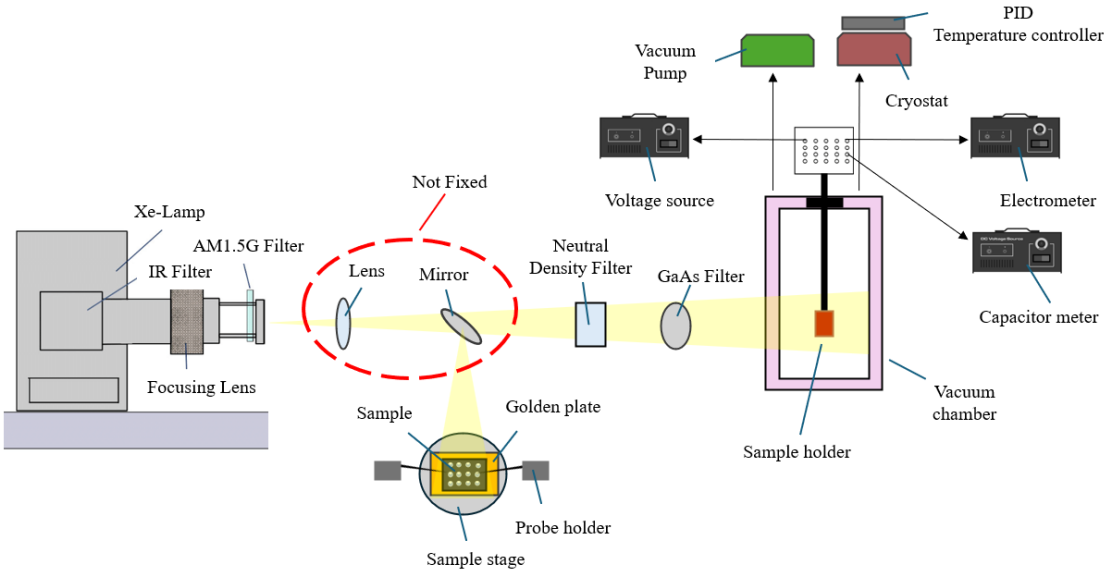

Figure 4. 4: *Schematic of the setup used for the acquisition of J-V characteristics under AM1.5G spectrum conditions. The beam can be focused on a probe station (below) or toward a vacuum chamber (left). Low temperature measurements were performed with this configuration.*

The condition used for JV measurements under dark conditions are given in *Table 4.1*. The values chosen for all the measurements carried out are based on previous works on similar devices.

Table 4. 1: *Measurement parameters used for the acquisition of the JV curves under dark conditions for each sample.*

Illumination Condition	*Start Voltage*	*Final Voltage*	*Step Bias*	*Averaged Samples*	*Delay after acquisition*
Dark	*-3* V	*3.5* V	*0.05* V	*3*	*400* ms

CV curves under dark conditions

The setup in *Figure 4.4* was also used for CV measurements under dark conditions. The samples are measured in the vacuum chamber and the capacity is measured with a 7200 Capacitor Meter (Boonton, New Jersey).

Capacitance-voltage measurements, performed with the objective to study how the unintentional doping concentration changes between samples, have been measured with the conditions given in *Table 4.2.*

Table 4. 2: *Measurement conditions used for the CV analyses for each sample.*

Start Voltage	*Final Voltage*	*Step Bias*	*Averaged Samples*	*Delay after acquisition*	*Initial delay*	*Scale*
-5 V	*3* V	*0.02* V	*50*	*3000* ms	*2* s	*20* pF

JV curves under illuminated conditions

The setup in *Figure 4.4* allows to measure JV curves under illumination. For this purpose, the light source is a 1000 W-Xe-Arc Lamp (Newport, California) with the spectrum shown in *Figure 4.5* (black line). An Air Mass Filter 1.5 Global (AM1.5G) (Newport, California) is placed downstream of the Xe-lamp. It modifies the emission spectrum coming from the lamp to obtain the AM1.5G spectrum, as shown in *Figure 4.6*. The light from the lamp can be directed towards a probe station, allowing direct measurements at room temperature, or towards the vacuum chamber for measurements as function of temperature. In the former case, the samples do not require the bonding on a sample holder and the path of the light is focused through a set

of mirrors and lenses positioned in the setup. Moreover, lenses and mirrors can be moved in and out of the beam path allowing also for measurement in the vacuum chamber, where the diodes are exposed to the AM1.5G illumination through a quartz window.

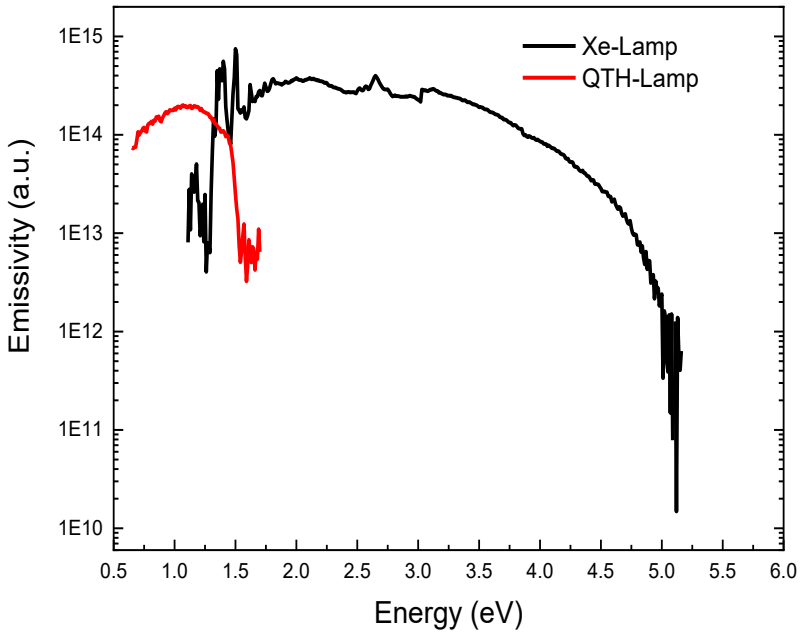

Figure 4. 5: *Emission spectra for the lamps used in the different setups. Xe-Lamp (black line), QTH-Lamp (red line).*

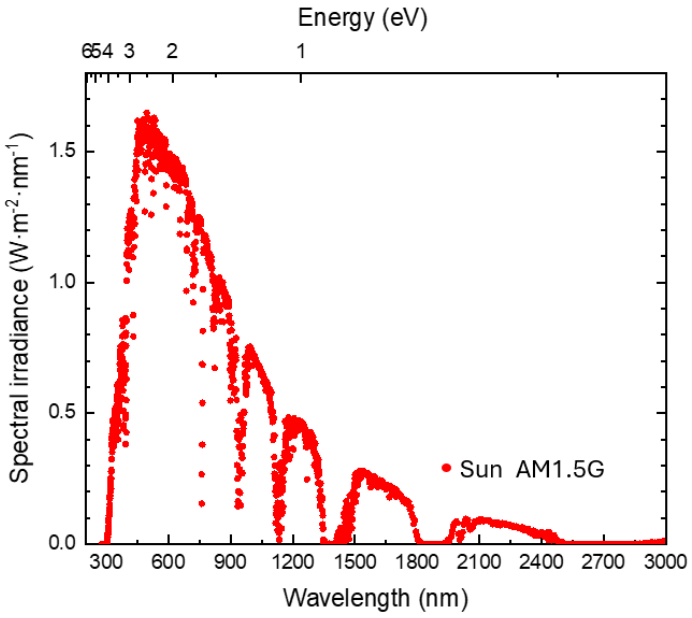

Figure 4. 6: *Transmitted Xe-Lamp spectrum behind the AM1.5G filter.*

Once the light passed through the AM1.5G filter it also passes through a neutral density filter, used to reduce the initial power of the beam (230 mW/cm^2) obtaining a power of 85 mW/cm^2). The neutral density (ND) filter used is a Reflective UV Fused Silica ND filter (ThorLabs, New

Jersey) with an optical density (OD) equal to 0.4 (for the measurement in the vacuum chamber) and 0.3 (for the analysis in the probe station). In this thesis light power of 85 mW/cm^2 is used to represent 1 sun condition (100 mW/cm^2), while light power of 230 mW/cm^2 is used to represent the 2 suns condition (200 mW/cm^2).

For some of the measurements carried out in this thesis, a GaAs filter was added to the setup. It is an undoped GaAs wafer mounted on a support lens holder that cuts of light of energy above the GaAs bandgap (1.42 eV = 873.24 nm).

The measurements under illumination are named as: 1 sun AM1.5G, 2 suns AM1.5G, 1 sun AM1.5G with GaAs filter, 2 suns AM1.5G with GaAs filter. They are illustrated in *Figure 4.7.*

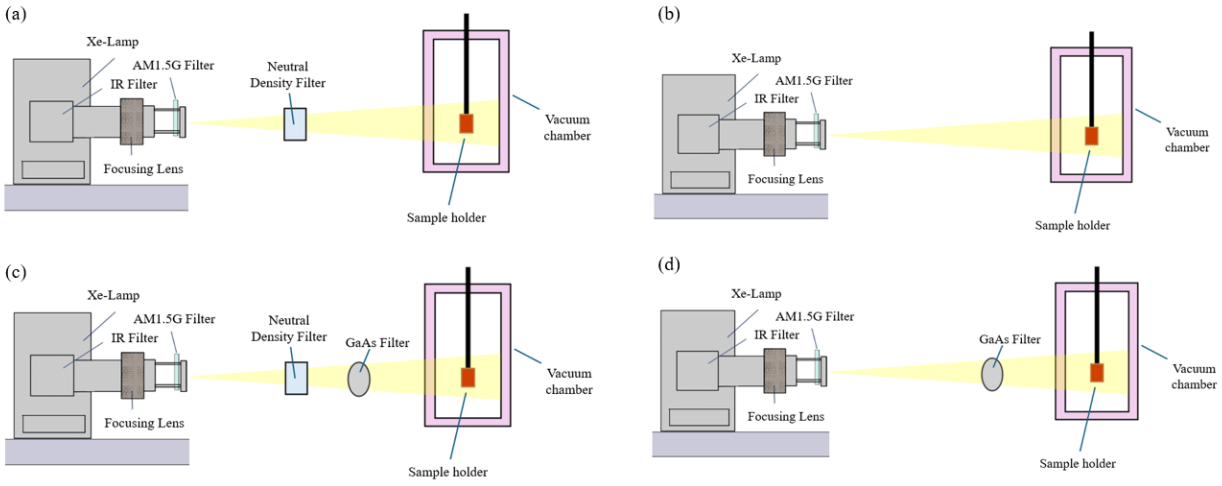

Figure 4. 7: *Illustration of the four different conditions used for bright measurements. (a) 1 sun AM1.5G solar spectrum. (b) 2 suns AM1.5G solar spectrum. (c) 1 sun AM1.5G solar spectrum with GaAs filter. (d) 2 suns AM1.5G spectrum with GaAs filter.*

Measuring a JV curve under AM1.5G conditions superimposes contributions from the GaAs bulk material and the QD-CL system to the photocurrent. To exclusively study the contribution of the QD/CL system, the setup needs to be modified such that carriers are only generated in the QDs. This is achieved by adding a GaAs wafer to the illumination path (*Figure 4.7(c-d)*) that absorbs the high energy part of the AM1.5G spectrum with energies above or equal to the GaAs bandgap. The remaining light that hits the sample can only excite carriers in the QDs/CL. Any current measured in this configuration must therefore originate within and be extracted from the QDs. A representation of the effect of the GaAs filter on the AM1.5G solar spectrum is shown in *Figure 4.8*. In all six previous conditions the main figures of merit were analysed. To calculate efficiency under these conditions, the power of the incident radiation must be known. Since this is a non-standardized measurement, the light intensity of the beam actually

transmitted by the GaAs filter is unknown. Therefore, the efficiency, under these conditions, is expressed in arbitrary units.

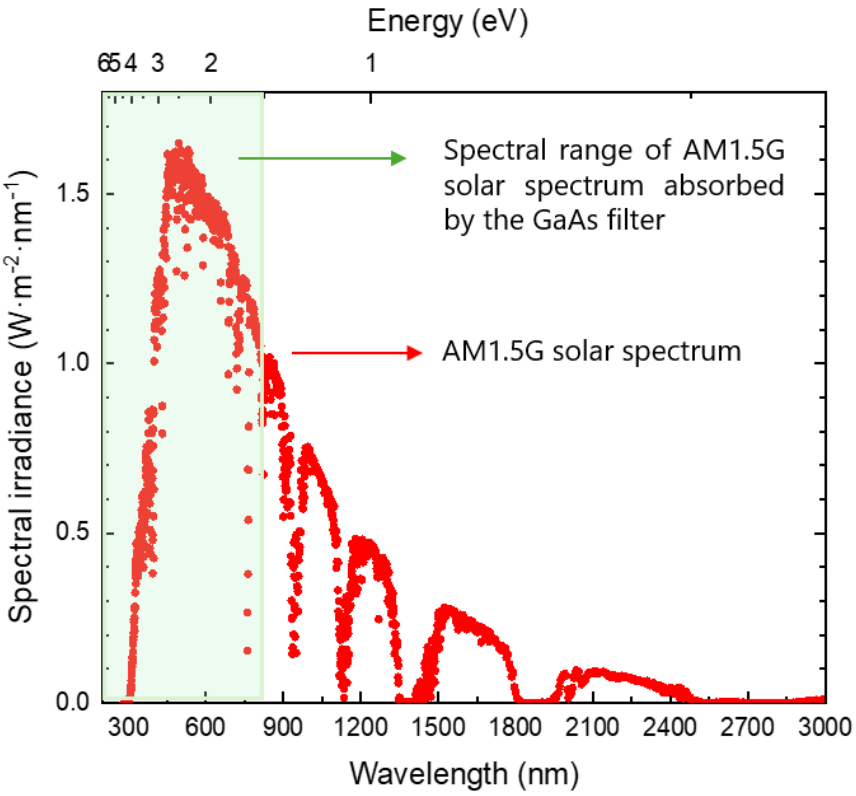

Figure 4. 8: *Solar irradiation spectrum of AM1.5G, 1 Sun (red line) and absorption of a GaAs filter.*

The parameters used for JV measurements under illuminated conditions are given in *Table 4.3.*

Table 4. 3: *Measurement parameters used for the acquisition of the JV curves under illuminated conditions for each sample*

Illumination Condition	*Start Voltage*	*Final Voltage*	*Step Bias*	*Averaged Samples*	*Delay after acquisition*
Bright	*0* V	*2.5* V	*0.01* V	*3*	*400* ms

4.3.2 Photocurrent spectroscopy setup

Photocurrent spectroscopy (PC) was performed over the four samples at room temperature. PC is a technique that measures the current generated and extracted from the device under test as a function of the energy of the monochromatic incident light. For the particular case of solar cells, PC analyses can determine how materials of different bandgaps in the cell contribute to the photogenerated current. Hence, PC allows to determine the photogenerated current from QDs, CLs and the host GaAs. In *Figure 4.9* the setup employed to measure photocurrent spectroscopy is shown.

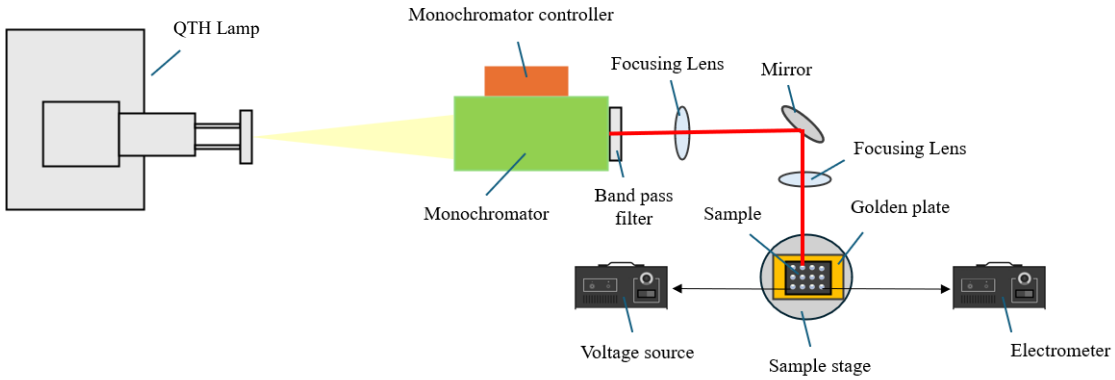

Figure 4. 9: *Sketch for the setup used for the acquisition of photocurrent spectra. The QTH lamp emits light that pass through a monochromator which divides the different wavelength as function of diffracted angle and selects a single wavelength. A band pass filter acts on the monochromatic light to filter the overlapping of spectral orders. A series of optical elements allows to focus the light on a sample stage on the probe station.*

A Quartz Tungsten Halogen (QTH) Lamp (Oriel Corporation, Stratford) with a spectrum plotted in *Figure 4.5* (red line) is used.

Further, a SPEX 0.34 m focal distance grating spectrometer (Edison, New Jersey) is mounted. Once the light passed through the monochromator, a long pass filter is used, to filter the overlapping of spectral orders. The monochromatic light leaving the SPEX monochromator is then directed towards a probe station as shown in *Figure 4.9.*

The measurements are performed placing the samples in the probe station. For these measurements, the voltage is applied and controlled using a K2401 Keithley (Keithley, Ohio) voltage source and the current is measured with a K6514 Keithley (Keithley, Ohio) electrometer.

From the data on PC, the External Quantum Efficiency (EQE) can be calculated as follows. The spectral photo-generated current is converted into responsivity dividing by the power per unit area of the QTH lamp [14]. The spectral responsivity of the sample is given by:

$$R_\lambda = \frac{I_\lambda}{P_\lambda}, \qquad \textit{Eq. 4.1}$$

where I_λ is the spectral photogenerated current and P_λ the spectral power of the light source. Then, the responsivity is converted to EQE by multiplying by the photon energy divided by the electron charge, as given in the *Equation 4.2* [14,30].

$$EQE = R_\lambda \frac{h\nu}{q}, \qquad \textit{Eq. 4.2}$$

where h is the Planck's constant and ν the frequency of the monochromatic light.

The conditions used for all the PC measurements are the ones listed in *Table 4.4*

Table 4. 4: *Measurement conditions used for the PC spectroscopy for each sample.*

Initial Energy	*Final Energy*	*Energy Increment*	*Averaged samples*	*Delay after acquisition*
0.7 eV	*1.6* eV	*0.01* eV	*3*	*400* ms

5. Results and discussions

This chapter contains measurement results and a discussion of the performed experiments. For each sample, five diodes were measured, so for simplicity, a representative diode for each sample was selected for analysis, assuming a common average behaviour among all. Room temperature (RT) JV measurements in dark and various illuminated conditions, CV profiling, and photocurrent spectroscopy are analysed. Furthermore, measurements as function of temperature are studied. The latter focus on carrier dynamics in the semiconductor, and on the effects related to the type-I and type-II band alignment.

The samples studied in this work are S-Sb_0, S-Sb_5, S-Sb_17 and S-Sb_22. They are analysed based on how the amount of Sb in the capping layer alters the properties of the QDSCs. All the samples have the same structure, as shown in *Figure 4.1*, the only difference is the amount of Sb in the capping layer. A simplified illustration of the measured samples is given in *Figure. 5.1.*

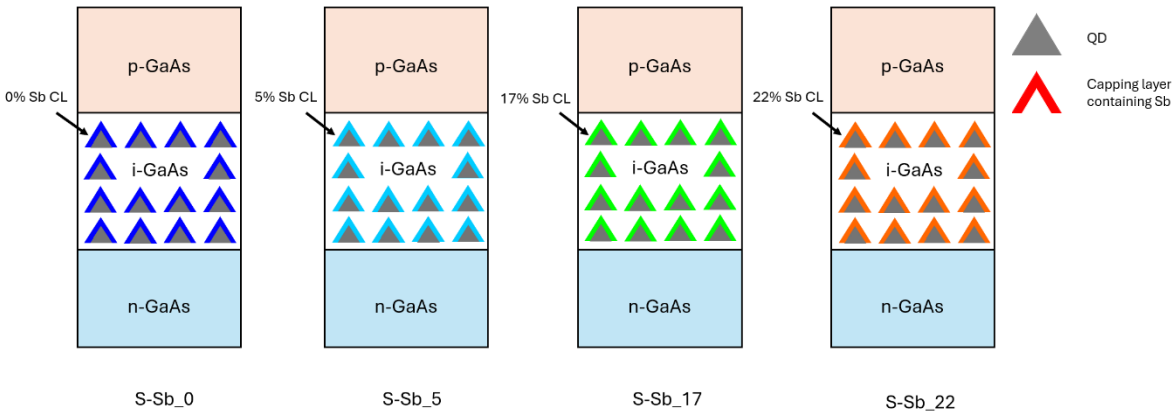

Figure 5. 1: *Sketch of the four samples analysed in this work. The percentage of Sb used in the CL is indicated.*

As explained in Chapter 3, the content of Sb in the CL significantly influences the electronic band structure of barrier material. Hence, differences in the band alignment for each sample are expected.

In S-Sb_0, the presence of a GaAs CL does not change the band alignment. However, due to the In-Ga intermixing the QD height reduces. The reduction in size determines a high energy band gap (*Equation 2.3*). Moreover, a strong overlapping in the electron and hole wavefunctions and short radiative lifetime is expected.

By adding 5 % of Sb, the band alignment is still expected to be type-I, but the GaAsSb CL affects the GaAs valence band by increasing its energy level. With the rising valence band

offset, holes move towards the QD edges, increasing carrier lifetime and extraction efficiency (two steps process). A 5% content of Sb is not enough to fully prevent the QD dissolution, however a reduction in the energy gap, if compared with S-Sb_0, is expected.

Finally, in the S-Sb_17 and S-Sb_22 samples, the content of Sb exceeds the 14-16% threshold, as previously highlighted in *Section 3.4*. In these two samples type-II band alignment is expected. Because of the transition, the radiative lifetime further increases. Instead, the extraction efficiency and the energy band gap of the nanostructure decreases. Despite their similarity, in S-Sb-17 the barrier energy for the holes is lower than in S-Sb_22.

5.1 Room temperature characterization

In this section the results obtained from room temperature measurements are presented and discussed.

5.1.1 Current – voltage characteristics in dark conditions

Dark JV curves for a representative diode of each sample are shown *Figure 5.2*. An important observation is the significant discrepancy between the reference sample (S-Sb_0) and the others in the reverse bias conditions. Examining the forward bias region, it is observed that the mismatch persists at low biases. Then, for biases above 0.5 V, the JV curves overlap, and all samples follow a similar trend. Saturation current, shunt and series resistances have been derived from the JV curves under dark conditions, fitting the one-diode model (*Equation 2.3*) to the measurement data. They are reported in *Table 5.1.*

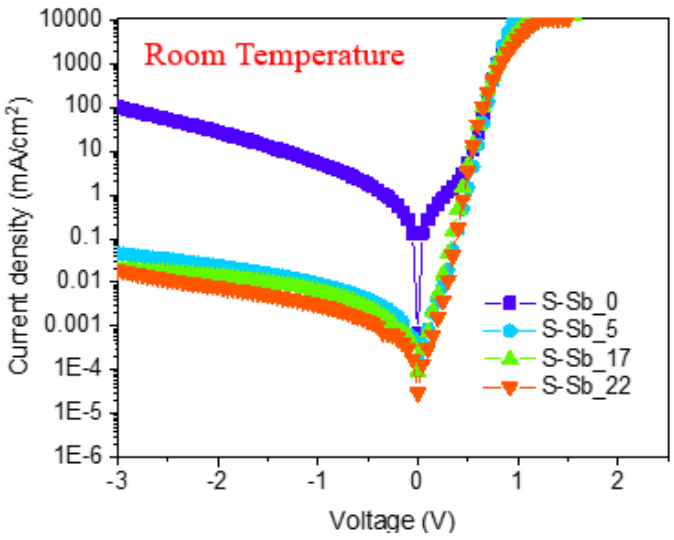

Figure 5. 2: *JV characteristics in dark conditions at room temperature for the four samples under analysis.*

Table. 5. 1: *Saturation current, shunt and series resistances extracted from dark JV curves at room temperature.*

Sample	Saturation current [10^{-6} mA/cm^2]	Shunt resistance [kΩ/cm^2]	Series resistance [Ω/cm^2]
S-Sb_0	454.81	0.33	0.38
S-Sb_5	24.90	139.05	0.53
S-Sb_17	49.30	285.60	0.12
S-Sb_22	2.43	358.94	0.24

A correlation is observed between the high saturation current and the shunt resistance in sample S-Sb_0. Specifically, the shunt resistance in sample S-Sb_0 is three orders of magnitude lower, and the saturation current is an order of magnitude higher in the reference sample compared to the values derived for the other three samples. For the series resistance, no significant variations are observed among the four samples.

Based on this analysis, the high saturation current can be attributed to manufacturing-induced defects in the analysed diode of the S-Sb_0 sample. In particular, these defects could be attributed to an imperfect wire soldering process (for this sample), which creates alternative channels for current flow, bypassing the p-i-n junction. The presence of these channels facilitating charge flow, also explains the low shunt resistance in the case of the reference sample. While these imperfections leave clear traces in the dark JV characteristics of S-Sb_0,

they have a minor impact under strong illumination. Therefore, S-Sb_0 is nonetheless kept in the analysis hereinafter.

Since a solar cell operates in forward bias, hence the performance-limiting factors under positive bias are particularly important. Information regarding recombination can be examined through *Figure 5.3(a-b),* which respectively depict the local ideality factors and the global ideality factor for each sample. The local ideality factor is given by the slope of the forward biased JV curves. Instead, the global ideality factor of the device is extracted from the minima of the local ideality factor curves. As explained in Section 2.3, the ideality factor is a parameter related to recombination process within the devices [89,90-91]. It decreases monotonically with increasing Sb content from 2.06 for S-Sb_0 to 1.32 for S-Sb_22.

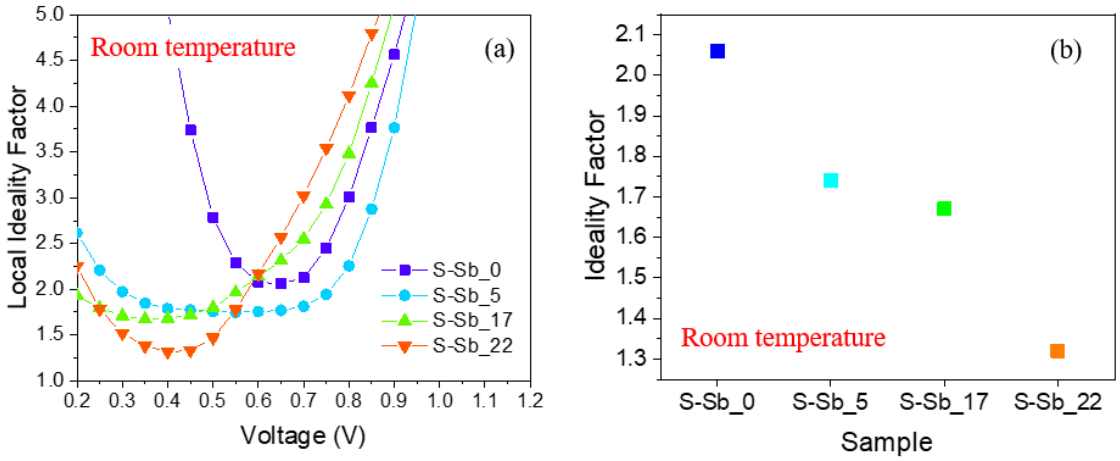

Figure 5. 3: *(a) Local ideality factor for the four different samples at room temperature. (b) Ideality factor for the four different samples at room temperature.*

In QDSCs at room temperature, two different recombination mechanisms are possible [89]. As illustrated in *Figure 5.4,* when a forward bias is applied, the quantum dot layers positioned at the edge of the space charge region are likely to be occupied by majority carriers from the adjacent region. This occupancy can lead to the trapping of carriers of opposite polarity, resulting in recombination (mechanism 1). Recombination for the quantum dots in the centre of the quasi-neutral region occurs through the simultaneous capture of an electron and a hole by the same quantum dot (mechanism 2) [89].

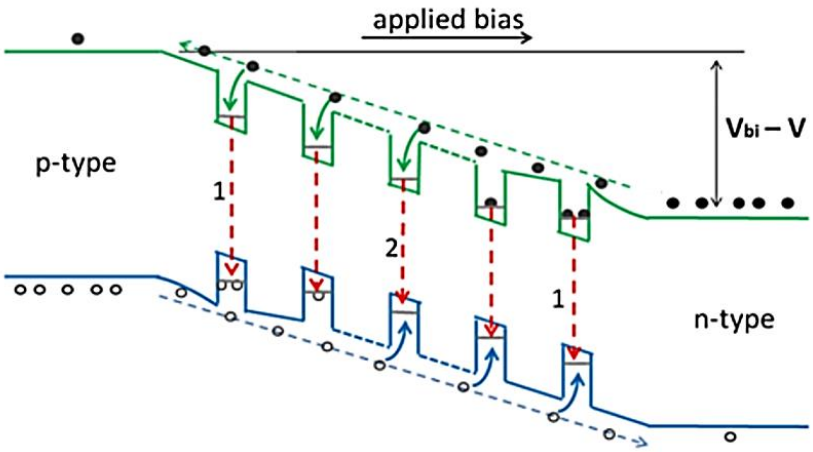

Figure 5. 4: *Illustration of the two recombination mechanisms involved in QDSCs at room temperature. (1) recombination mechanism at the edges of the SCR. (2) recombination mechanism in the middle of the SCR [89].*

The second mechanism has the requirement of the simultaneous capture of carriers, and it resembles defect-related recombination found in the depletion region of a standard solar cells, which typically results in an ideality factor around 2 [17,89,90-91]. All carriers involved in the diffusion current under forward bias must cross the depletion region. By assuming that the possibility of charge trapping is independent of the Sb content in the CL, mechanism 2 should be pronounced similarly across all samples. However, carriers escape through thermal excitation does depend on the Sb content in the CL.

In type-I structures (S-Sb_0 and S-Sb_5), holes can be thermally exited out of the QDs by a one or two step process (through the CL), respectively [73]. This extraction promotes the movement of carriers jumping in and out of the QDs, which reach the middle of the space charge region and recombine following mechanism 2. Hence, ideality factors equal to 2 are reasonable.

As Sb content increases, the wavefunctions of the holes become more localized within the capping layer of the quantum dots, resulting in a type-II band structure. Due to the type-II band alignment, the QD-CL hinders the escape of holes, opposed to type-I. Hence, the SCR edges can be assumed to be permanently filled by majority holes and, recombination mechanism 1 is more expressed, leading to lower ideality factors for the type-II samples [89]. This is a first indication that carrier transport through the SCR is strongly affected by the GaAsSb CL for high Sb contents.

5.1.2 Capacitance – voltage profiling

Capacitance – voltage profiling was performed at room temperature on the four samples. In *Figure 5.5* the apparent doping profiles for the different structures are shown.

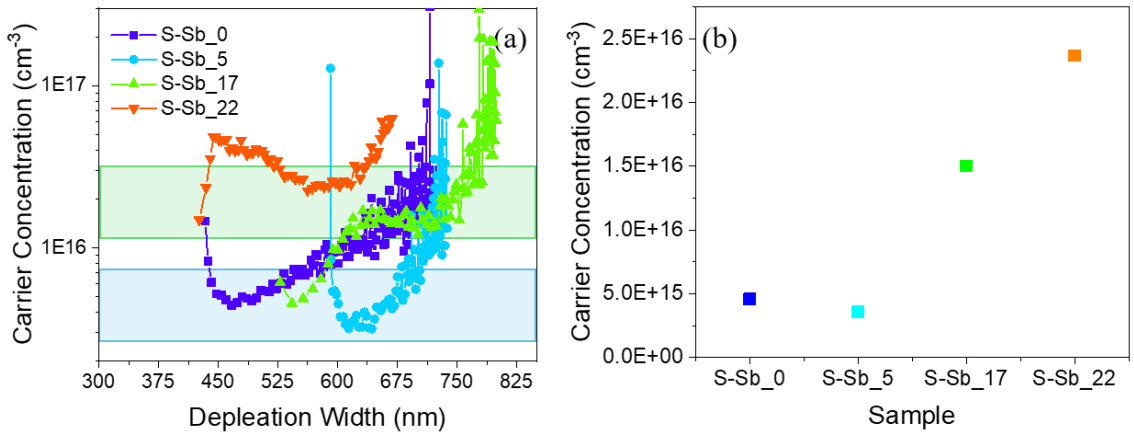

Figure 5. 5: *(a) Apparent doping profiles for the diodes analysed. The colourful bands indicate, qualitatively, where the minima of the U-shaped curves fall. The carrier concentration is extracted from this region. (b) Mean unintentional doping concentrations for each sample.*

The carrier concentration extrapolated from these plots has been extracted from the minimum of each curve (according to the discussion in Section 2.4). Type-II structures of high Sb content show clearly higher UID levels than type-I samples (with less and without Sb). UID doping is not directly related to the QDs as a source of free carriers. The 10 equally spaced layers should correspond to a QD density of about $3x10^{11}$ cm^{-3} [30]. This value is 4 to 5 orders of magnitude lower than the UID measured for type-I and type-II structures, respectively.

Consequently, the excess of carrier concentration must originate from defects. On the one hand, the GaAsSb CL should reduce the strain between InAs-QDs and the overgrown GaAs, corresponding to a reduced UID concentration in S-Sb_5 with respect to S-Sb_0. However, very high Sb contents lead to highly strained structure resulting in the formation of point defects (S-Sb_17) and extended defects (S-Sb_22), as depicted in *Figure 3.10* [77]. With the simulations from Section 2.4, flat-potential regions can therefore be expected in S-Sb_17, and even more in S-Sb_22. Accordingly, based on the UID measured for these structures, a lower carrier collection efficiency and thus losses in J_{SC} are expected for these structures.

5.1.3 Photocurrent spectroscopy

Sample S-Sb_5, S-Sb_17 and S-Sb_22 are analysed through photocurrent spectroscopy. From these, the external quantum efficiency percentage was derived, and it is here presented in *Figure 5.6.* The study of photocurrent spectroscopy for sample S-Sb_0 was not feasible due to the high saturation current, as discussed previously.

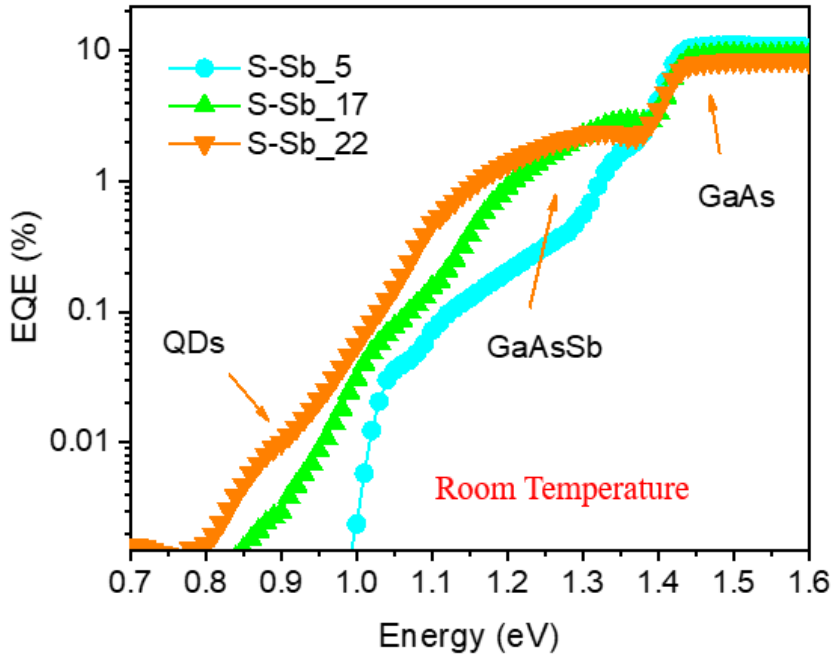

Figure 5. 6: *EQE spectra at room temperature for samples with 5%, 17% and 22% of Sb in the CL. The different contributions from GaAs, QDs and CLs are indicated for sample S-Sb_22 as an example.*

The results shown in Figure 5.6 are in agreement with expectations [77,92]. Increasing the percentage of Sb, the absorption edge progressively shifts towards lower energies. In the sample containing 22% of Sb, the width of the spectrum is maximized, allowing absorption above 1.55 µm (~ 0.8 eV). A significant difference can be found between the spectra associated with the type-II structure and the one associated with the type-I band alignment. In the latter case, absorption is limited to energies greater than 0.98 eV. The spectra in the *Figure 5.6* show two characteristic shoulders for each spectrum. These correspond to the contribution of the CL [77], which evidently varies with the concentration of Sb.

Across all samples, the EQE saturates for energies above 1.42 eV, where the contribution of QD-CL systems is overshadowed by the background material, GaAs, which possess a band gap equals to 1.42 eV. It is also observed that increasing the concentration of Sb, the EQE above 1.42 eV decreases from 11.1%, in S-Sb_5 to 8.4%, in S-Sb_22, at 1.5 eV. This effect can be

correlated with the previously obtained results for UID. The higher the concentration of Sb, the higher the concentration of unintentional doping and defects, which reduces the carrier collection efficiency by reducing electric field – assisted extraction (see Section 2.4).

By integrating the area under each spectrum, in *Figure 5.6*, for energies below 1.42 eV, it is possible to discriminate the contribution of GaAs from the QD-CL systems. It is found that the integrated photocurrent for sample S-Sb_17 is 1.59 % greater than that of sample S-Sb_22, which in turn is 6.78 % greater than that of S-Sb_5. As expected, due to the smaller absorption range, the photocurrent generated in type-I structures is lower compared to that in type-II structures. However, in the case of the sample with 17% of Sb, the photocurrent is slightly higher than in S-Sb_22 despite the larger energy gap. This can be explained by considering the two competing processes playing a role in type-II structures. On one hand, a higher Sb content results in a lower energy gap and a broader absorption range. On the other hand, as the Sb content increases, the energy barrier for hole escape also increases, hindering carrier extraction. Moreover, higher UID in the S-Sb_22 also limits carrier extraction.

In conclusion, photocurrent spectroscopy allows us to underline two results. Firstly, the absorption range is extended with higher Sb contents. However, the increased photocurrent energy range going from 17% to 22% of Sb, does not compensate for this substantial carrier collection efficiency losses, that are inherent to high Sb content.

5.1.4 Current – voltage characteristics under illumination

JV curves under different illumination conditions are analysed.

1 sun AM1.5G illumination

Figure 5.7(a-b) show the behaviour for the different samples under 1 sun AM1.5G illumination and 1 sun AM1.5G with GaAs filter illumination, respectively. In *Figure 5.7(b)* the JV curve for S-Sb_0 is not reported. Under these illumination conditions, the photogenerated current density is insufficient to overcome the unusual high dark current density flowing in the low bias region, due to low shunt resistance.

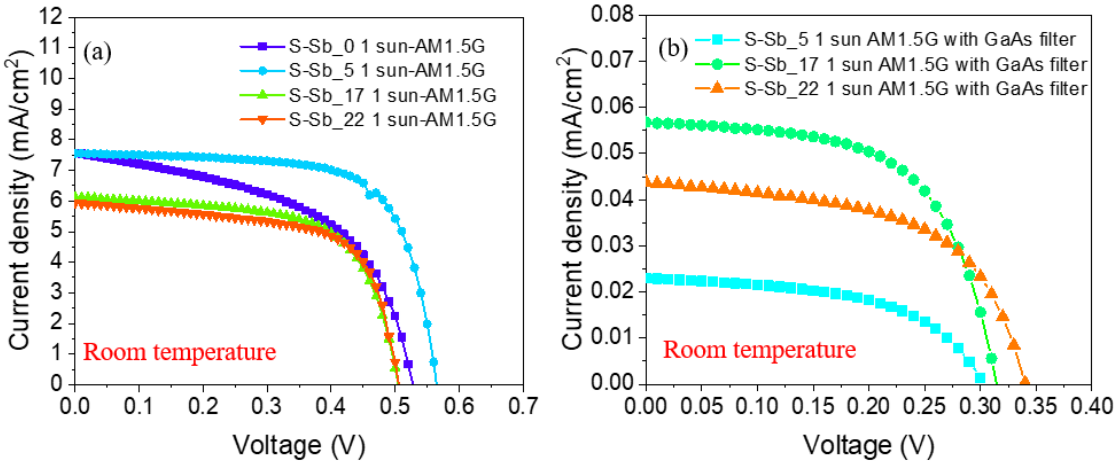

Figure 5. 7: *(a) JV characteristics at room temperature under 1 sun AM1.5G conditions. (b) JV characteristics at room temperature under 1 sun AM1.5G with GaAs filter conditions.*

In *Table 5.2* the one-diode model parameters extracted from JV measurements under dark conditions, 1 sun AM1.5G and 1 sun AM1.5G with GaAs are summarized.

Table. 5. 2: *Parameters extracted from JV curves under dark, 1 sun AM1.5G and 1 sun AM1.5G conditions. V_{OC}* is the open-circuit voltage calculated (from J_0, ideality factor and J_{SC}) using the one-diode model (Equation 2.5).*

	S-Sb_0	S-Sb_5	S-Sb_17	S-Sb_22
J_0 [10^{-6} mA/cm^2]	454.81	24.90	49.30	2.43
R_{SH} [kΩ/cm^2]	0.33	139.05	285.60	358.94
R_S [Ω/cm^2]	0.38	0.53	0.12	0.24
Ideality factor	2.06	1.76	1.67	1.32
1sun AM1.5 J_{SC} [mA/cm^2]	7.56	7.55	6.12	5.94
1 sun AM1.5G V_{OC} [V]	0.53 ± 0.01	0.56 ± 0.01	0.50 ± 0.01	0.51 ± 0.01
1 sun AM1.5G V^*_{OC} [V]	0.50	0.55	0.48	0.49
1 sun AM1.5G +GaAs J_{SC} [mA/cm^2]	-	0.02	0.06	0.04
1 sun AM1.5G +GaAs V_{OC} [V]	-	0.30 ± 0.02	0.31 ± 0.02	0.34 ± 0.02
1 sun AM1.5G +GaAs V^*_{OC} [V]	-	0.30	0.30	0.32

By analysing *Table 5.2* the following aspects are noteworthy.

Under 1 sun AM1.5G illumination, V_{OC} slightly increases when 5% of Sb is added to the CL. A further increase in Sb shows a reduction of the V_{OC}. Analogously, the J_{SC} shows higher values at lower Sb concentrations.

S-Sb_5 in contrast with S-Sb_0 benefits from reduced strain inside QDs, less defects and increased radiative lifetime which explains the higher V_{OC}. The facilitated extraction (two steps process) and the lower UID does not pronounce in a higher J_{SC}. However, samples S-Sb_17 and S-Sb_22 suffer from significantly more UID and defects, as well as a higher extraction barrier. Therefore, important extraction losses reduce the J_{SC}, and V_{OC} is lost through non radiative recombination [77,93-94-95], despite the type-II longer radiative lifetimes. In conclusion 5% of Sb in GaAsSb CL is the optimal content for 1 sun AM1.5G illumination, thus in application in a SJSC.

1 sun AM1.5G illumination with GaAs filter

The use of GaAs filter allows to discriminate the contribution from the QDs by suppressing the GaAs absorption contribution. JV curves measured with GaAs filter are shown in *Figure 5.7(b)*. The orders of J_{SC} and V_{OC} between samples are different from what has been seen under the full spectrum (*Figure 5.7(a)*). Here, S-Sb_5 has the lowest J_{SC}, which increases when Sb is added. The J_{SC} reaches its maximum value when 17% of Sb is used in the GaAsSb CL. Regarding the V_{OC}, under these conditions, the maximum V_{OC} is obtained in S-Sb_22, followed by S-Sb_17 and S-Sb_5.

The higher short-circuit current obtained for type-II systems can be explained considering the extension of the QDs absorption in type-II structures to longer wavelengths (in Section 5.3.1) [77]. Therefore, due to increased absorption, more current is generated. As discussed in the photocurrent spectroscopy analysis, the reasons why S-Sb_17 has a higher J_{SC} compared to S-Sb_22 are related to both the easier extraction (lower CL-barrier) and lower density of defects generated by the high concentration of Sb, which is higher in S-Sb_22.

The trend in the V_{OC} can be explained with the dark current. For low intensity illumination, dark current plays an important role which affects the JV curves under AM1.5G with GaAs filter. *Figure 5.8* shows the difference between dark current and photogenerated current under 1 sun AM1.5G and 1 sun AM1.5G with GaAs filter conditions. The two yellow areas represent the photogenerated current in both illuminated conditions. Regarding the photogenerated current with the GaAs filter, in the case of S-Sb_5, S-Sb_17, and S-Sb_22, the dark current becomes higher than the photogenerated current at voltages between 0.30 and 0.35 V. This illustrates how the differences in dark current between the different samples directly translate to the open-circuit voltage at such low illumination.

It can be concluded that the contribution from the QD-CL system is improved in type-II samples with moderate Sb contents, due to the larger radiative lifetimes and an acceptable level of defects. Nevertheless, the overall performance under AM1.5G conditions is degraded due to the detrimental effect that QD layers have on the current photogenerated in the GaAs due to carrier trapping, as shown in the PC spectra (*Figure 5.6*).

This analysis indicates that a promising Sb content for a potential application in MJSCs is 17%, due to the small contribution of UID and the long type-II radiative lifetime.

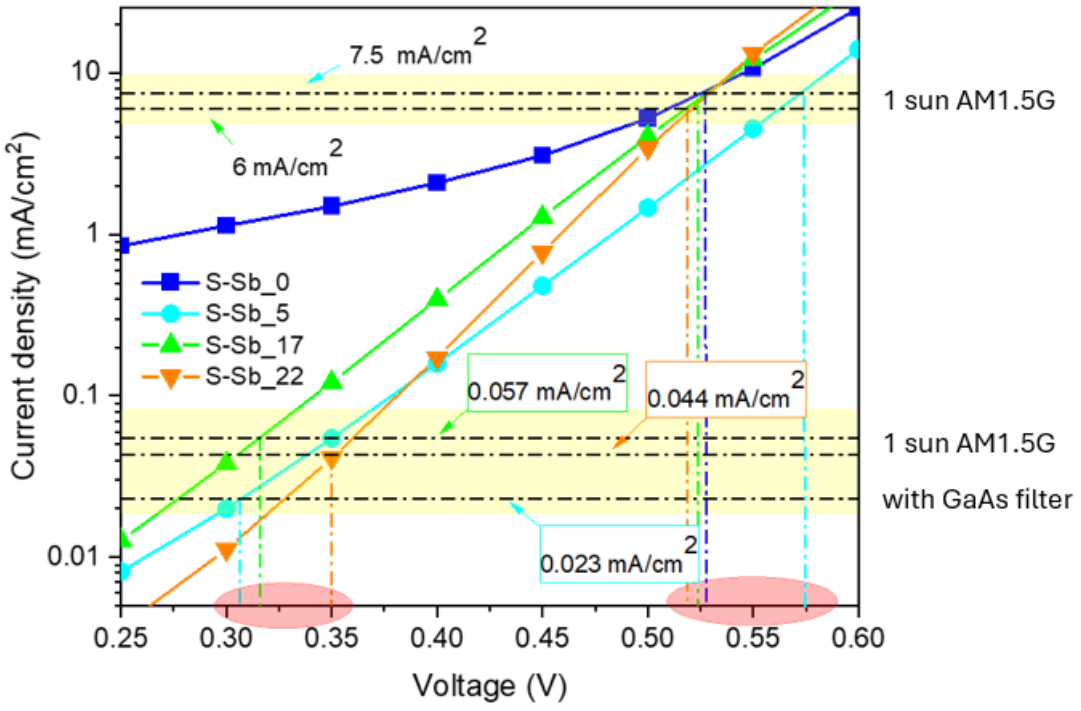

Figure 5. 8: *Magnification of dark JV curves of each sample, for a low-bias region. The yellow areas indicate the short-circuit current produced by each sample under two different conditions (1 sun AM1.5G and 1 sun AM1.5G with GaAs filter). The red circles, at the bottom, represent the open-circuit voltages of the diodes.*

2 suns AM1.5G illumination

The behaviour of the diodes was also analysed under the 2 suns AM1.5G spectrum, shown in *Figure 5.9*. A significant increase in photocurrent is observed when transitioning from 1 sun to 2 suns illumination. With higher intensity, the photogenerated current is more than doubled. Additionally, comparing these two sets of measurements, a slight increase in V_{OC} is also observed when the light-power increases.

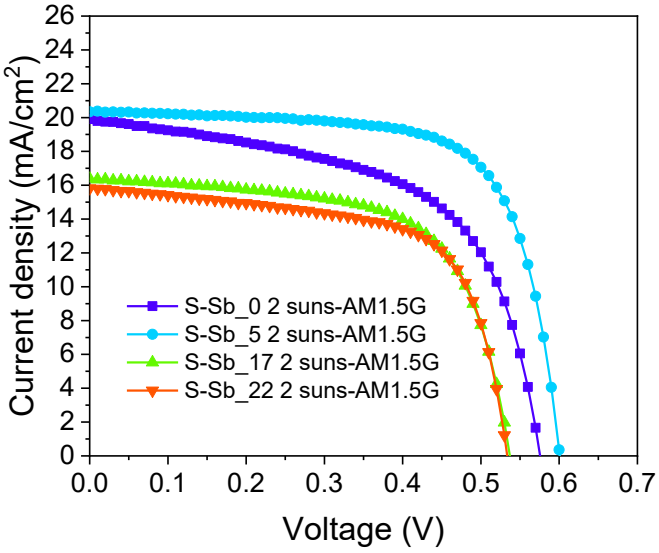

Figure 5. 9: *JV characteristics at room temperature under 2 suns AM1.5G conditions*

Common key performance indicators obtained under 1 sun AM1.5 and 2 suns AM1.5 illuminations are given in *Figure 5.10.*

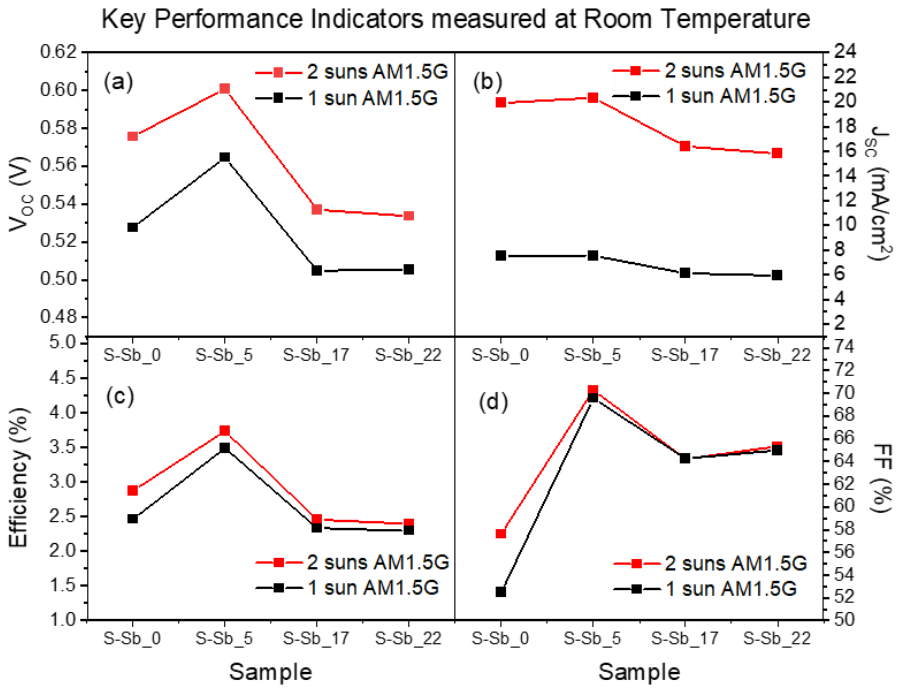

Figure 5. 10: *Open circuit voltage (a), short-circuit current density (b), efficiency (c) and fill factors (d) for each sample at RT under 1 sun AM1.5G (black line) and 2 suns AM1.5G (red line).*

For all the systems studied, increasing the light intensity results in an increment in conversion efficiency. However, type-II structures are less affected by this enhancement than type-I structures. Sample S-Sb_0 shows the maximum enhancement, with the efficiency increasing by

about 17%, while, in S-Sb_22 the efficiency increases by about 4%. The higher efficiency under 2 suns can be explained by assuming that by doubling the incident power, the QDs absorb photons and generate electron-hole pairs more frequently. The higher frequency of these processes leads to a saturation of the QD's ground states. For a QD, to act as a recombination centre, it must capture an electron and a hole. However, if QDs are constantly packed with charge carriers due to high illumination and overall high carrier density, they cannot act as traps anymore, resulting in less recombination and overall higher efficiency. In type-II structures the saturation is faster because of the longer lifetime, which increases as the content of Sb in the CL increases [73,96]. Hence, type-II systems are already affected by the saturation of the QDs due to their band structure and the enhancement in the efficiency, as result of more impinging power, is limited. The reason why the efficiency increases more in S-Sb_0 than in S-Sb_5, both type-I structures, is related to the effect of the increased FF *(Figure 5.10(d))*.

The efficiency enhancement coming with the increase in the power going, from 1 sun to 2 suns, makes QDSCs a potential candidate for applications in concentrator solar cells (CSCs).

Conclusions for measurements at room temperature

From the analyses at room temperature, it can be concluded that:

- High Sb content in the GaAsSb CL comes with high concentration of UID that results in low carrier collection efficiencies.
- GaAsSb CL extends the absorption range (up to 1300 nm in type-I and beyond 1500 nm in type-II). However, the higher UID and the energy barrier for holes in the CL reduce the carrier extraction efficiency.
- 5% of Sb maximises the power output for an application in a SJSC. This is due to an extended absorption range and an improved carrier collection.
- 17% of Sb maximises the contribution from the QDs. This is due to a further extended absorption range, longer lifetimes and the overall material quality being preserved.
- 5% of Sb maximises the power output for an application in a CSC. This is due to a faster carrier extraction from the type-I alignment with respect to type-II structures, where QDs are saturated.

5.2 Characterization as function of the temperature

Samples S-Sb_0, S-Sb_5, S-Sb_17 and S-Sb_22 are measured as a function of temperature under dark, 1 sun AM1.5G and 2 suns AM1.5G conditions. Moreover, samples with a GaAsSb capping layer are analysed also under 1 sun AM1.5G and 2 suns AM1.5G with the GaAs filter. For these measurements, the temperature was reduced down to 25 K. A schematic illustration indicating all analysed temperature steps is shown in *Figure 5.11*.

Figure 5. 11: *Schematic Illustration for the temperature's steps used in this work.*

5.2.1 Current – voltage characteristics under dark conditions

JV curves under dark conditions are used to extract parameters as a function of temperature. Four parameters are analysed: the ideality factor, the reverse saturation current and the shunt and series resistances. Particular attention is given to the ideality factor, being directly correlated to the recombination mechanisms [17,38]. *Figure 5.12* illustrates the main features and corresponding investigation regions derived from the analysis of dark JV curves as a function of temperature.

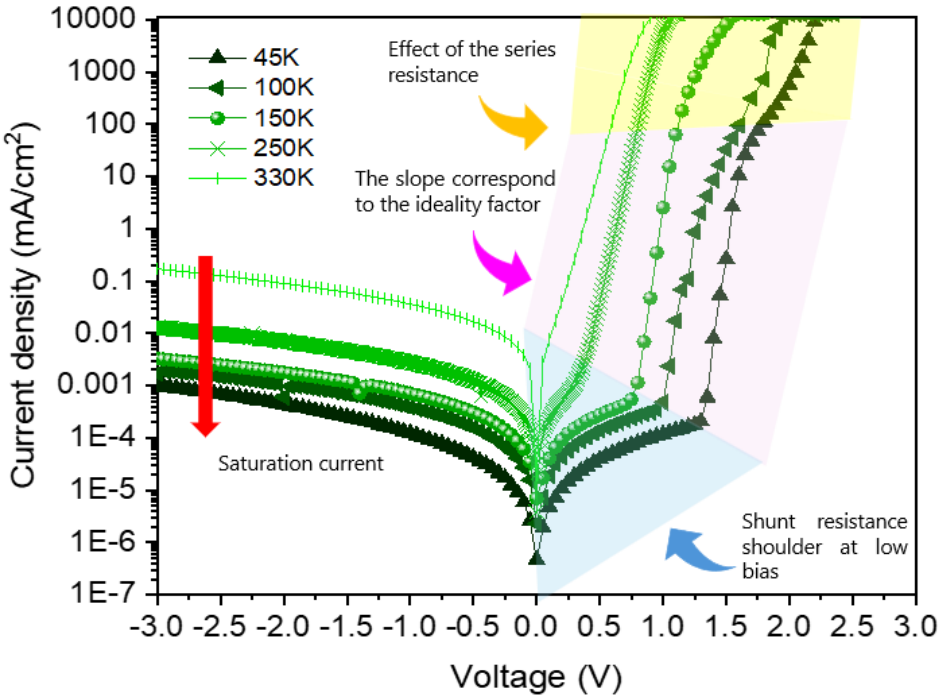

Figure 5. 12: *Example of experimental dark JV curves measured as a function of temperature. The yellow area shows the region where series resistance becomes relevant; the pink area is the region where the ideality factor is calculated by measuring the slope of the curve; the blue triangle indicates the region where the effect of modified carrier transport mechanisms emerges due to the presence of QDs; the red arrow shows the expected reduction in saturation current as the temperature decreases.*

A feature that is present in all the samples are low bias shoulders. These shoulders become more pronounced at low temperature. The reason is that at low temperatures, the kinetic energy of forward-injected carriers is reduced and may be too small to overcome the potential of the p-i-n junction [89]. As a result, the voltage required to see a substantial change in the current increases progressively with temperature. Moreover, in QDSCs, the quantum dots in the depletion region create an additional potential barrier (*see Figure 5.4*). This barrier is formed by the occupation of the QDs and, due to the poor thermal excitation at low temperatures, carrier escape towards the contacts of the cell is reduced [89]. This overpotential barrier inhibits the forward injection of carriers, so that the dark current requires a higher bias to show a substantial increase in current.

In *Figure 5.13* the dark JV measurements as a function of temperature for S-Sb_0, S-Sb_5, S-Sb_17 and S-Sb_22 are shown. Unfortunately, for S-Sb_17, the shift of the voltage where no net – current flows (in *Figure 5.13(d)*) have made the acquisition of data difficult. This is the reason why in *Figure 5.13(c)* the plotted results for this sample end at 200 K.

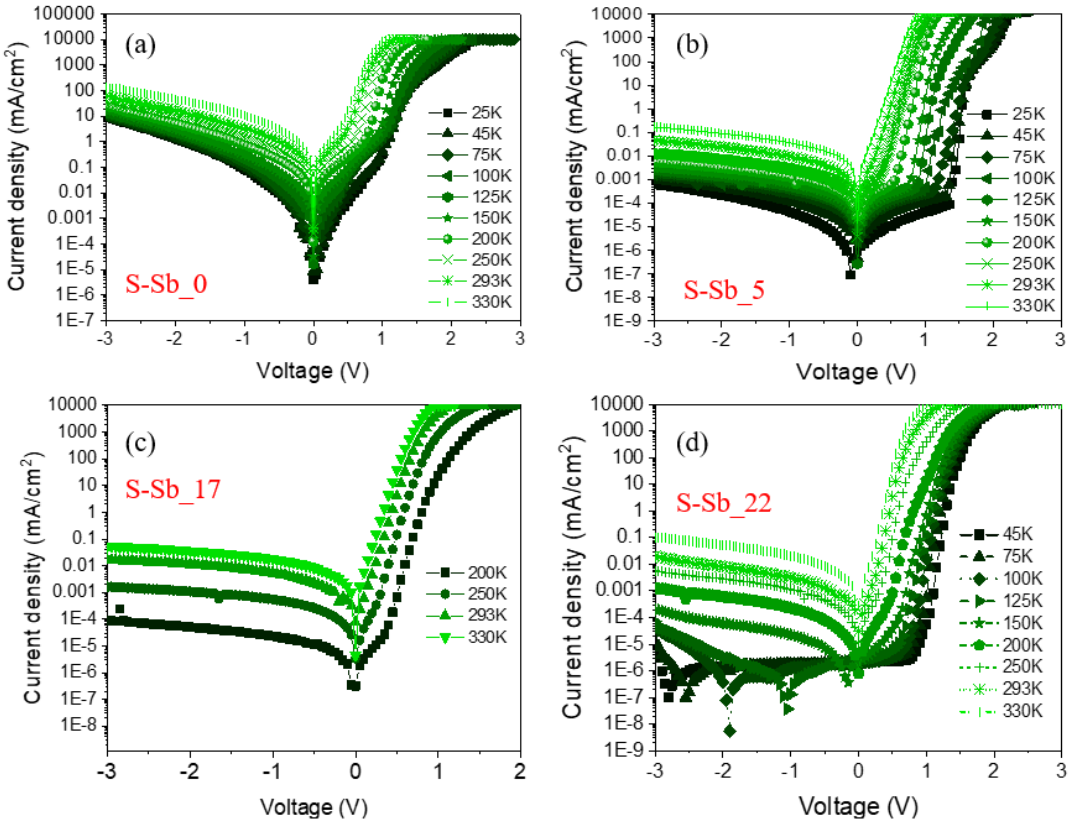

Figure 5. 13: *Dark JV curves as function of the temperature for the reference sample (a), for the sample with 5% of Sb in the GaAsSb CL (b), for the sample with 17% of Sb in the GaAsSb CL (c), for the sample with 22% of Sb in the GaAsSb CL (d).*

For all samples, the dark current is reduced at lower temperatures. This is mainly due to the exponential temperature dependence of the intrinsic carrier concentration (*Equation 2.6).* In addition, sample S-Sb_0, S-Sb_5 and S-Sb_22 present the onset of a shoulder in forward bias range when the temperature reduced below 150 K. This shunt resistance-related effect could be associated with changes in the transport mechanisms. At high temperature, thermal excitation allows a continuous process of trapping and detrapping of carriers. Therefore, under these conditions, QDs can be considered as effective traps for carriers. However, when the temperature decreases, the ability of carriers to be thermally extracted decreases and the occupation increases. Hence, at low temperatures, the trap-like recombination through the QDs is reduced.

Focusing on the reverse saturation region for S-Sb_22, the devices shows a "*normal*" diode JV characteristic in dark conditions down to 200 K. Below this temperature, the diode shows two anomalies. The voltage corresponding to zero net- current shifts progressively towards negative

biases instead of remaining at 0 V. This feature can be related to transient effects, due to the presence of defects in the p-i-n diode. However further analysis must be done to accurately explain this artefact. The second anomaly is the slope of the saturation current, which increases abruptly when the diode operates below 200 K.

The ideality factors for the four samples have been extracted from dark measurements and reported in *Figure 5.14*.

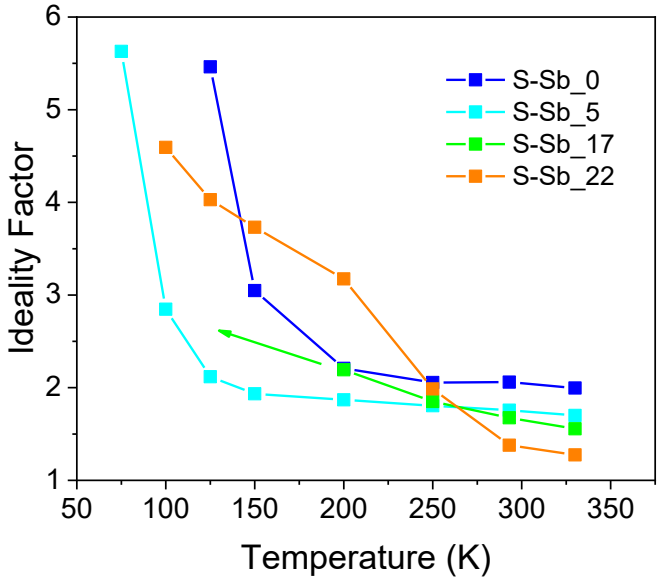

Figure 5. 14: *(blue line) Ideality factor in a range of temperature between 330 K and 125 K for the reference sample. (cyan) Ideality factor in a range of temperature between 330 K and 75 K for the sample with 5% of Sb in the GaAsSb CL. (green line) Ideality factor in a range of temperature between 330K and 200 K for the sample with 17% of Sb in the GaAsSb C, the green arrow indicates the linear increase supposed. (orange line) Ideality factor in a range of temperature between 330K and 100 K for the sample with 5% of Sb in the GaAsSb CL.*

In type-II samples, the ideality factor increases linearly reducing the temperature and becomes greater than 2 for relatively high temperatures (200 K). In type-I samples the ideality factor remains constant (~ 2) in a wider range of temperatures. Then, at 150 K (S-Sb_0) and 100 K (S-Sb_5), the ideality factors exceed 2.

If n has values between 1 and 2, the current flow is given by diffusion-recombination current [89,90-91]; while, if n is larger than 2, a tunnelling mechanism dominates [91,97-98]. It has been commonly accepted that an ideality factor larger than 2 is a typical feature of a defect-assisted tunnelling current [97-98-99-100-101]. Indeed, if the concentration of intermediate levels is sufficiently high in the band gap the SCR, carriers will tunnel following a staircase route. This mechanism is known as "*diagonal tunnelling*" [98]. A schematic illustration of this

tunnelling processes is given in *Figure 5.15.* Therefore, the main factor driving this tunnelling mechanism are the defects with states in the middle of the energy gap [75,91,102].

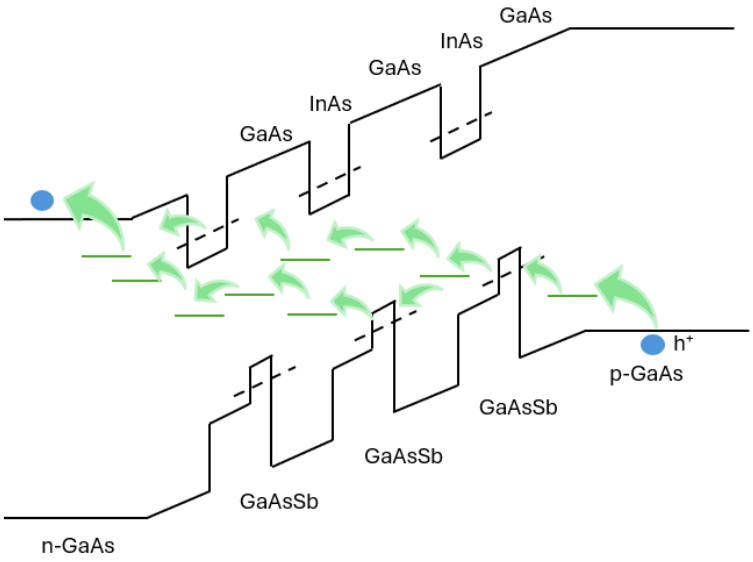

Figure 5. 15: *Schematic illustration defects assisted tunnelling process for a type- II structure. The green line, in the middle of the band gap, indicate defect states. The arrows show a hypothetical path for a hole (blue ball on the left) in the p-type GaAs to cross in the n-type GaAs. In this process ground states in the CL assist the tunnelling.*

It is important to consider the information provided by the CV profiling. S-Sb_0 is affected by a higher UID than S-Sb_5, hinting towards a higher defect density. This could be the reason why the ideality factors seem to be less affected by the temperature when 5% of Sb is added in the GaAsSb CL. On the other hand, type-II structures show one order of magnitude higher UID than type-I. Therefore, the higher concentration of defects will promote the tunnelling mechanism, leading to a linear increase in the ideality factor with temperature.

Furthermore, a contribution from the nanostructures in the intrinsic region is possible. The energy states of the QDs could contribute to the tunnelling process acting as additional "stairs" promoting carrier flow. In type-II structures the ground state of the holes is shifted to the CL with an energy higher than in the case of type-I band alignment. Hence, these states act more properly as defect-like states in the middle of energy band gap.

This could be the reason why the effect is predominantly observed in type-II structures. Further investigations are needed, to confirm this hypothesis.

By observing the ideality factors as a function of temperature plotted in *Figure 5.14*, the S-Sb_17 shows a linear trend, and it diverges from the standard ideality factors values (between

1 and 2) starting from 200 K. Confirming that, if tunnelling affects carrier transport in S-Sb_22, it similarly affects S-Sb_17, both being type-II structures.

From the results obtained it can be concluded how samples with type-I band alignment behave different from the type-II structures. The different characteristic features of type-I and type-II are related to the variation in the band alignment of the nanostructures embedded in the intrinsic layer of the QDSCs. In the next paragraphs, further information on these structures will be extracted considering the JV characteristics under illumination.

5.2.2 Current – voltage characteristics under AM1.5G spectrum

Figure 5.16 shows the JV curves, under 1 sun AM1.5G, for the four samples.

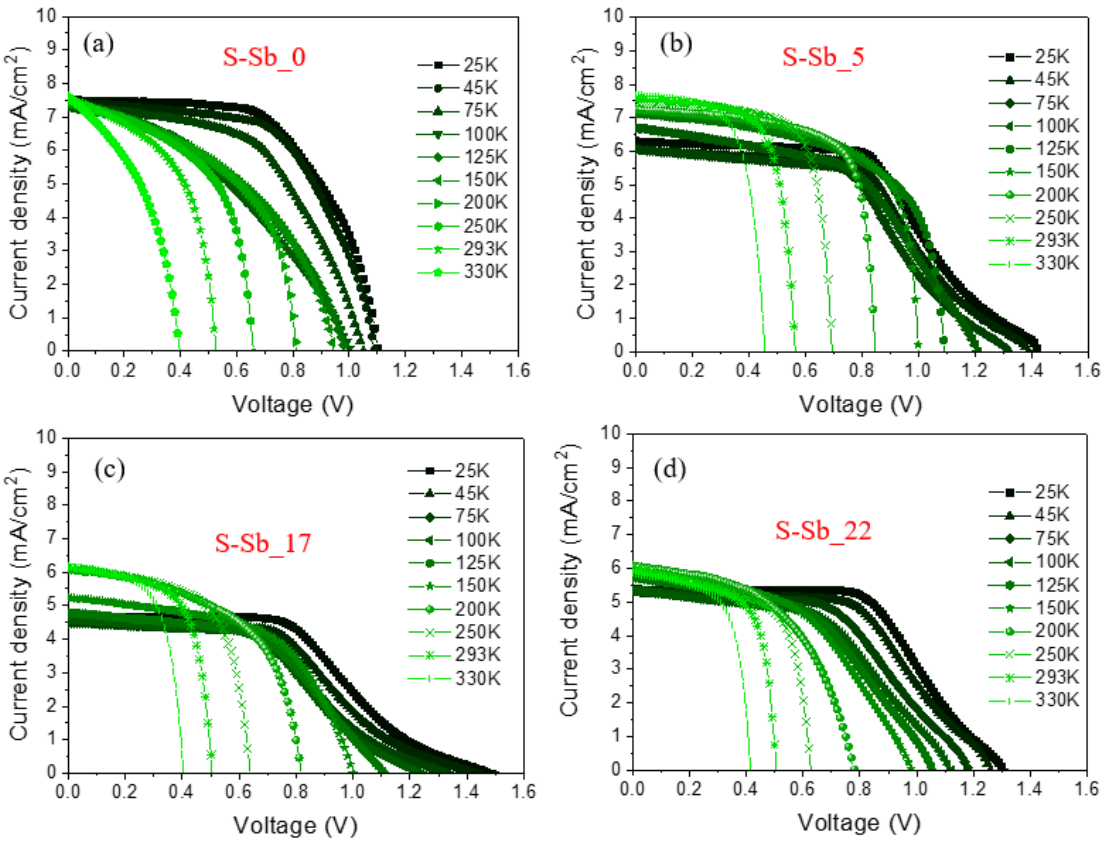

Figure 5. 16: *JV curves as function of the temperature obtained under 1 sun AM1.5G for the reference sample (a), for the sample with 5% of Sb in the GaAsSb CL (b), for the sample with 17% of Sb in the GaAsSb CL (c), for the sample with 22% of Sb in the GaAsSb CL (d).*

All the KPIs as function of temperature, for the four samples, obtained under 1 sun AM1.5G are represented in *Figure 5.17*. The prominent observations going to lower temperature are: an

increasing V_{OC} and a decreasing J_{SC} for Sb samples below 200K. This results in an increasing efficiency when going to lower temperatures.

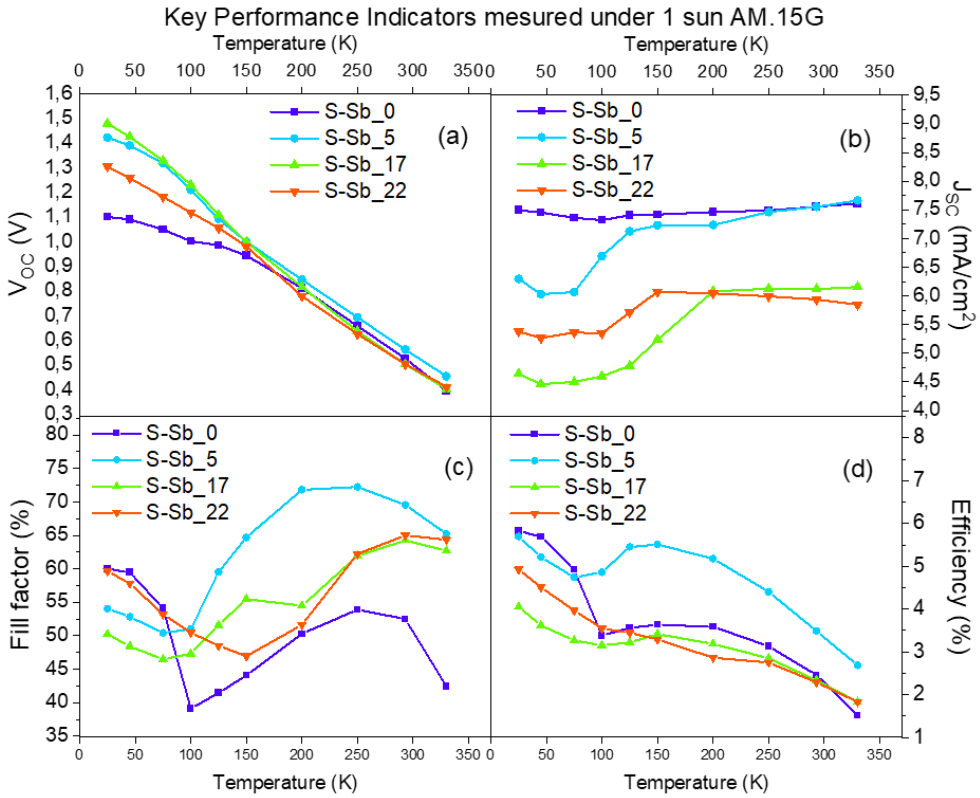

Figure 5. 17: *(a) Open-circuit voltage as function of temperature for each sample under 1 sun AM1.5G. (b) Short-circuit current as function of temperature for each sample under 1 sun AM1.5G. (c) Fill factor (%) as function of temperature for each sample under 1 sun AM1.5G. (d) Efficiency (%) as function of temperature for each sample under 1 sun AM1.5G.*

Analysing the V_{OC} evolution in more detail, the increasing trend can be explained with *Equation 2.5* and *Equation. 2.6*. The former relates the V_{OC} to the inverse of the saturation current, while the latter demonstrates how the saturation current depends on the intrinsic carrier concentrations and the diffusion coefficients of holes and electrons. Therefore, the V_{OC} inversely depends on these two parameters which shrink with decreasing temperature [17]. Moreover, the V_{OC} directly dependents on the energy gap of the material, which increases when the temperature decreases [17]. These relationships explain why V_{OC} generally increases when temperature decreases.

The samples are compared with each other in *Figure 5.17(a)*. At first, the V_{OC} increases linearly across all samples by decreasing the temperature. However, below 150K, the trends diverge. The V_{OC} increases sublinearly for S-Sb_0, linearly for S-Sb_22 and superlinearly for S-Sb_5 and S-Sb_17. These trends cannot be fully explained at this point.

Another noteworthy aspect is that at low temperatures, the V_{OC} of S-Sb_5 S-Sb_17 and S-Sb_22 exceeds the band gap of the QD-CL system. This implies that at low temperatures the electronic structure of the QDs does not affect the overall potential difference (V_{OC}) across the devices.

In *Figure 5.17(b)* the J_{SC} obtained under 1 sun AM1.5G, for the S-Sb_0, S-Sb_5, S-Sb_17 and the S-Sb_22 are shown. The samples with GaAsSb CL show a dip of about 15 % in J_{SC} when going below 150 K. It could be assumed that QDs no longer contribute to the photocurrent. However, the loss in J_{SC} exceeds the contribution of sub-GaAs absorption. Therefore, it is more likely that the 5 nm GaAsSb CL hinders efficient carrier transport at low temperature. This could be due to localized holes in the CL and formation of a potential barrier. The J_{SC} as function of temperature in S-Sb_0 does not show a reduction at low temperatures because the CL in this sample is free of Antimony.

Based on these results it can be concluded that the GaAsSb CL limits applications for SJSCs at very low temperatures.

5.2.3 Current – voltage characteristics under 1 sun AM1.5G with GaAs Filter

In *Figure 5.18* the JV curves for S-Sb_5, S-Sb_17 and S-Sb_22 under 1 sun AM1.5G with GaAs filter and for all the temperatures are shown.

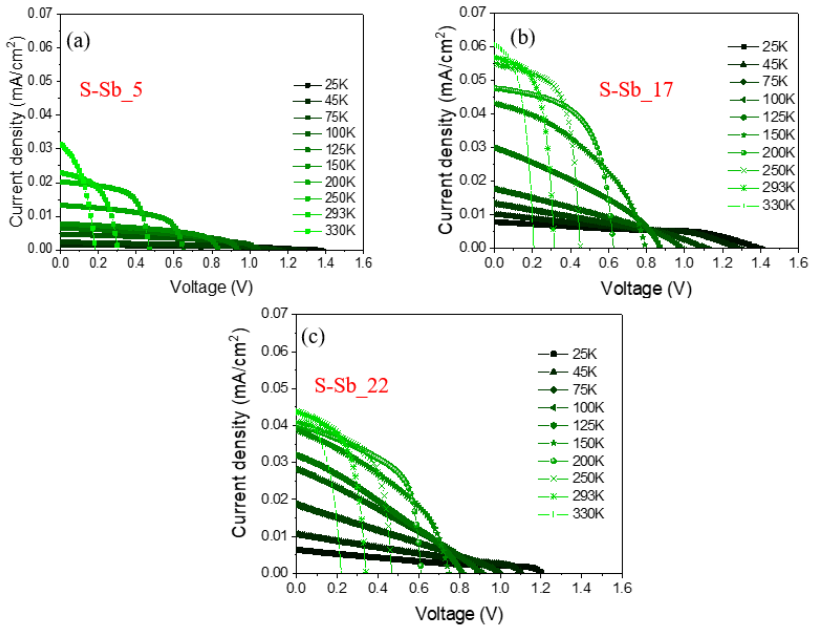

Figure 5. 18: *JV curves as function of the temperature obtained under 1 sun AM1.5G with GaAs filter for the sample with 5% of Sb in the GaAsSb CL (a), for the sample with 17% of Sb in the GaAsSb CL (b), for the sample with 22% of Sb in the GaAsSb CL (c).*

In this configuration, measurements provide direct information regarding absorption through and extraction from QDs and CL. All the KPIs measured under 1 sun AM1.5G with GaAs filter are depicted in *Figure 5.19*.

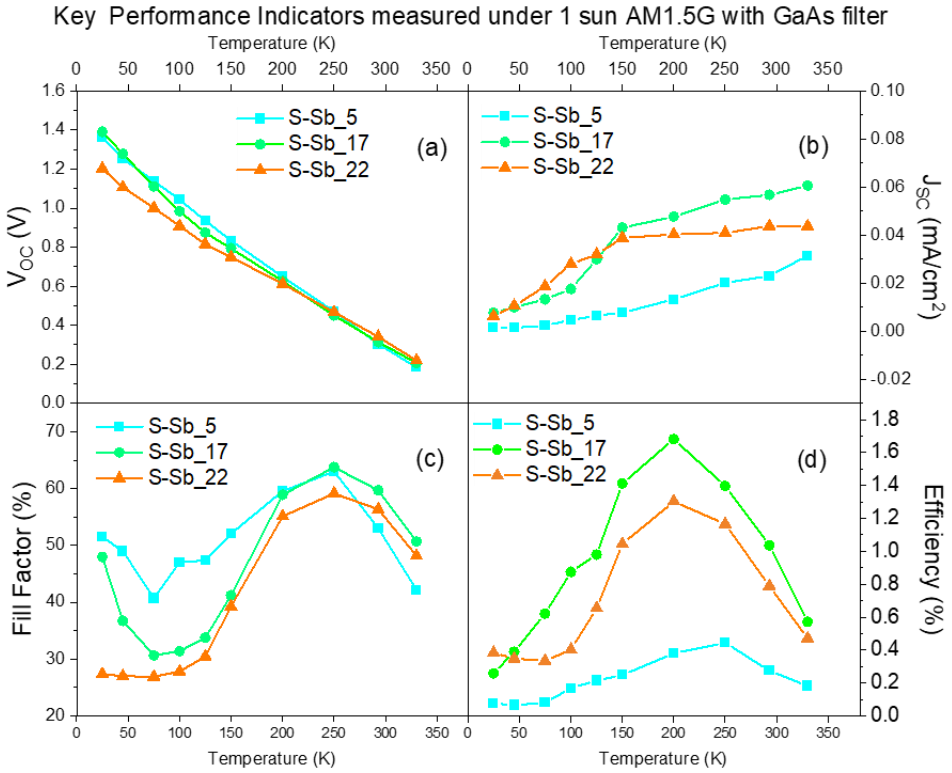

Figure 5. 19: *(a) Open-circuit voltage as function of temperature for each sample under 1 sun AM1.5G with GaAs filter. (b) Short-circuit current as function of temperature for each sample under 1 sun AM1.5G with GaAs filter. (c) Fill factor (%) as function of temperature for each sample under 1 sun AM1.5G with GaAs filter. (d) Efficiency (%), in arbitrary unit, as function of temperature for each sample under 1 sun AM1.5G with GaAs filter.*

Here, the V_{OC} increases linearly across all samples, as the temperature decreases. Regarding the J_{SC}, current decreases across all samples when going to lower temperatures. Below 150 K, there is a steep decay for the high Sb content samples (S-Sb_17 and S-Sb_22), so that all samples converge to about 0.005 mA /cm^2.

These findings are in agreement with what has been stated above: at low temperature QDs do not contribute to the photocurrent of a SJCSs anymore. At the same time, this makes them unsuitable for an application in a MJSC at very low temperatures. However, the inverse parabolic trend in the efficiency, with a peak at 200 K, makes them a candidate for applications in this temperature region, such as in low-Earth-orbit conditions.

5.2.4 Current – voltage characteristics under 2 suns AM1.5G

Figure 5.20 shows the KPIs for all the samples obtained under 2 suns AM1.5G.

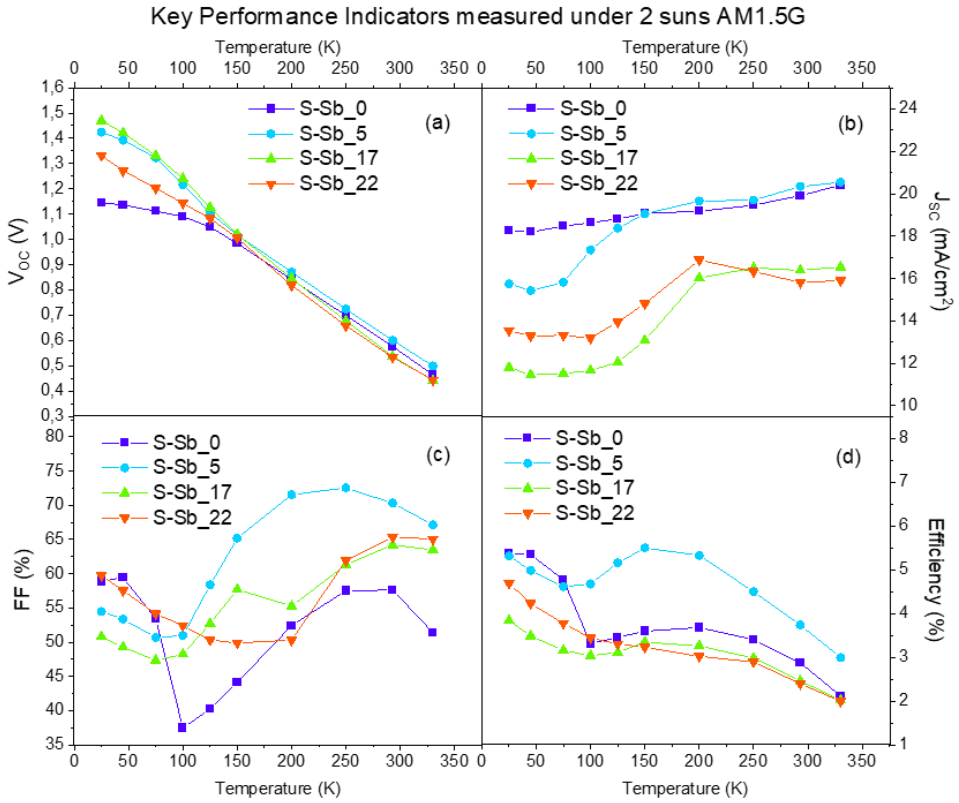

Figure 5. 20: *(a) Open-circuit voltage as function of temperature for each sample under 2 suns AM1.5G. (b) Short-circuit current as function of temperature for each sample under 2 suns AM1.5G. (c) Fill factor (%) as function of temperature for each sample under 2 suns AM1.5G. (d) Efficiency (%) as function of temperature for each sample under 2 suns AM1.5G.*

The tendencies for all the KPIs, with temperature, are the same as for 1 sun AM1.5G conditions.

The only noteworthy difference is found in the temperature evolution of the efficiency, shown in *Figure 5.21*.

In a range of temperatures between 330 K and 200 K, the efficiency of the QDSCs increases for higher illumination. This trend inverts when the temperature decreases below 200 K. This trend is observed for all the samples and it can be related to the reduced ability of carriers to be extracted at low temperatures.

For high temperatures the explanation is the one given in Section 5.1.4. Recombination becomes less dominant for saturated QDs. However, at low temperatures, carrier escape is reduced and the QDs cannot absorbed the increased photons flux. It can be concluded that the QDSCs under study could be an alternative for CSC only for medium-high temperature (200 - 350 K) applications.

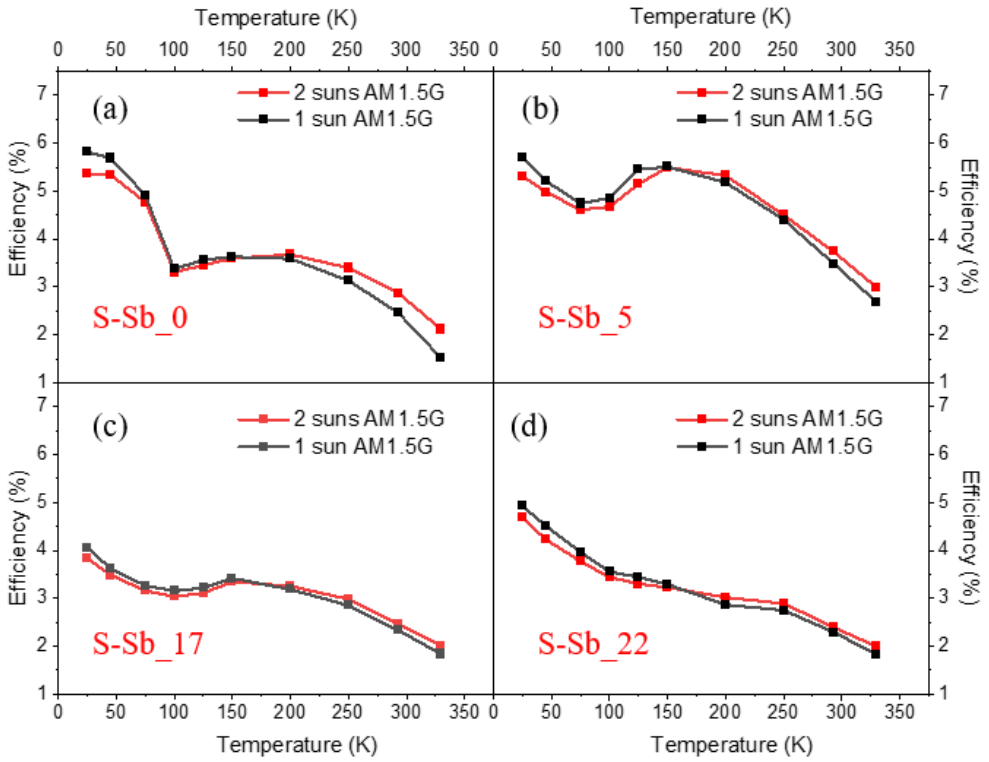

Figure 5. 21: *(a) Efficiency (%) for S-Sb_0 as function of the temperature under 1 sun AM1.5G (black line) and 2 suns AM1.5 (red line). (b) Efficiency (%) for S-Sb_5 as function of the temperature under 1 sun AM1.5G (black line) and 2 suns AM1.5 (red line). (c) Efficiency (%) for S-Sb_17 as function of the temperature under 1 sun AM1.5G (black line) and 2 suns AM1.5 (red line). (d) Efficiency (%) for S-Sb_22 as function of the temperature under 1 sun AM1.5G (black line) and 2 suns AM1.5 (red line).*

6. Conclusions and future work

Conclusions

This work investigated the influence of varying Sb concentrations in the capping layer on QDSCs, building upon existing knowledge while offering new insights into carrier dynamics and device performance.

The introduction of Sb significantly influences the band structure, reducing hole wavefunction overlap and enhancing radiative carrier lifetime, which also affects carrier extraction and recombination mechanisms through changes in the potential barrier for holes.

Room temperature characterization showed that higher Sb content in the GaAsSb capping layer increases light absorption (up to 1300 nm for type-I and beyond 1500 nm for type-II) but also introduces defects and potential barriers that reduce carrier collection efficiency.

Room temperature capacitance-voltage profiling confirms that higher Sb content correlates with higher unintentional doping levels, introducing imperfections.

For single-junction solar cells, 5% of Sb in the CL, optimizes power output by extending the absorption range without compromising carrier collection efficiency. Multi-junction solar cells prioritize a broad absorption range. In this case, 17% of Sb content in the CL offers the best performance, due to the extended absorption and potentially longer carrier lifetimes within tolerable material quality limits. Concentrator solar cells benefit from carrier extraction at high light intensities. Here, 5% of Sb in the CL proves optimal performance, suggesting faster extraction in type-I structures outweighs potential lifetime gains in type-II QDs under high illumination.

Temperature-dependent analysis reveals complex transport mechanisms, with type-II QDSCs showing a stronger tunnelling tendency influenced by defect states. Current – voltage analysis at different temperatures suggests diminishing QD contribution to current below 150 K when GaAsSb CL is added. Based on these results it can be concluded that the GaAsSb CL limits applications for SJSCs and MJSCs at very low temperatures. Nevertheless, MJSC are a candidate for applications in low-Earth-orbit conditions.

Future work

Future works should focus on optimizing growth conditions to reduce defects for Sb contents between 5% and 17%. Subsequentially, the same optoelectronic characterization conducted in this thesis must be performed on the new samples (with Sb between 5 and 17%) to confirm the obtained results and expand the understanding of these systems.

Additionally, it is necessary to select a reference sample (no Sb in the CL) with a lower dark current, allowing the analyses of this system under low injection conditions, which allows to investigate the properties of QD-CL systems.

Further research to refine the understanding of QDSC physics are needed, including:

- in-depth photoluminescence studies as a function of temperature and experiments with single-layer QD samples to better understand emission, absorption, and transport dynamics of these systems;
- variation in the position of the QDs layers within the intrinsic region to modulate carrier population;
- introduction of other V-group elements in the CL, such as Nitrogen and Phosphorus, to improve the strain compensation;
- studies on structures with electronic coupling between QDs, to improve carrier dynamic.

7. References

[1] R. F. Curl, Richard E. Smalley Biographical Memoir, *National Academy of Sciences (2021)*. https://www.nasonline.org/publications/biographical-memoirs/memoir-pdfs/smalley-richard.pdf

[2] D.F. Carlo, Third generation solar cells: modeling and simulation*, Master Thesis, Politecnico di Milano, (2010)*. https://hdl.handle.net/10589/12342

[3] United Nations, Kyoto Protocol To The United Nations Framework Convention On Climate Change, *(1998)*: https://unfccc.int/sites/default/files/kpeng.pdf

[4] United Nations, Paris Agreement, *(2015):* https://unfccc.int/sites/default/files/english_paris_agreement.pdf

[5] United Nations Climate Change: https://unfccc.int/process-and-meetings/the-paris-agreement

[6] Energy transition outlook, *International Renewable Energy Agency (IRENA):* https://www.irena.org/Energy-Transition/Outlook

[7] Fossil Fuels, *Environmental and Energy Study Institute EESI, (2021)*: https://www.eesi.org/topics/fossil-fuels/description#:~:text=Fossil%20fuels%E2%80%94including%20coal%2C%20oil,were%20compressed%20and%20heated%20underground

[8] H. Ritchie, P. Rosado, Fossil fuels. *Our World in Data*, *(2017)*: https://ourworldindata.org/fossil-fuels

[9] Nuclear Power in a Clean Energy System, *IEA (2019)*: https://www.iea.org/reports/nuclear-power-in-a-clean-energy-system

[10] P. Nikolaidis, Solar Energy Harnessing Technologies towards De-Carbonization: A Systematic Review of Processes and Systems, *Energies*, 17, 6153 *(2023)*. https://doi.org/10.3390/en16176153

[11] F. J. M. M. Nijsse, J. Mercure, *et al*., The momentum of the solar energy transition. *Nature Communications*, 14, 6542 *(2023)*. https://doi.org/10.1038/s41467-023-41971-7

[12] Solar energy, *International Renewable Energy Agency (IRENA)*: https://www.irena.org/Energy-Transition/Technology/Solar-energy

[13] R. Gaspar, How Solar PV is Winning Over CSP, *Renewable Energy World, (2013)*: https://www.renewableenergyworld.com/storage/how-solar-pv-is-winning-over-csp/#gref

[14] A. G. Martín, Structures based on GaAs(Sb)(N) semiconductor alloys for high efficiency multi-junction solar cells, *Doctoral Thesis, Universidad Politecnica de Madrid*, *(2020)*. https://doi.org/10.20868/upm.thesis.57487

[15] P. Team, The biggest problems with solar power today, and how to solve them, *PVcase*, *(2024):* https://pvcase.com/blog/the-biggest-problems-with-solar-power-today-and-how-to-solve-them/

[16] B. Zaidi, Solar panels and photovoltaic materials, *InTechOpen, (2018)*. https://doi.org/10.5772/intechopen.72061

[17] P. Würfel, U. Würfel, Physics of Solar Cells: From Basic Principles to Advanced Concepts, In *Wiley-VCH, (2009).* https://ci.nii.ac.jp/ncid/BB22814640

[18] First practical silicon solar cell, *American Physical Society 125, (2009)*: https://www.aps.org/apsnews/2009/04/bell-labs-silicon-solar-cell

[19] D. Mariano, Ottimizzazione dei componenti di un sistema elettrochimico integrato per la valorizzazione della CO_2 alimentato ad energia solare, *Master Thesis, Politecnico di Torino, (2023).*

[20] S. Sharma, K. K. Jain, *et al.,* Solar Cells: In Research and Applications - A Review. *Materials Sciences and Applications*, 6, 1145–1155, *(2015)*. https://doi.org/10.4236/msa.2015.612113

[21] J. Pastuszak, P. Węgierek, Photovoltaic cell generations and current research directions for their development. *Materials*, 15, 5542, *(2022)*. https://doi.org/10.3390/ma15165542

[22] G. Brown, J. Wu, Third generation photovoltaics, *Laser & Photonics Reviews*, 3, 394–405, *(2009)*. https://doi.org/10.1002/lpor.200810039

[23] M. Grätzel, Dye-sensitized solar cells. *Journal of Photochemistry and Photobiology. C, Photochemistry Reviews*, 4, 145–153, *(2003)*. https://doi.org/10.1016/s1389-5567(03)00026-1

[24] S. Khalid, M. Sultan, *et al.,* Emerging Nanotechnologies for Renewable Energy, *Micro and Nano Technologies*, 3–35, *(2021)*. https://doi.org/10.1016/b978-0-12-821346-9.00019-5

[25] Photovoltaic research, *National Renewable Energy Laboratory (NREL)*: https://www.nrel.gov/pv/

[26] S. S. Indira, C. A. Vaithilingam, *et al.,* A review on various configurations of hybrid concentrator photovoltaic and thermoelectric generator system, *Solar Energy,* 201, 122-148, *(2020)*. https://doi.org/10.1016/j.solener.2020.02.090

[27] S.P. Philipps, S. P, A. W. Bett, III–V multi-junction solar cells, *The Royal Society of Chemistry,* 87–117, *(2014)*. https://doi.org/10.1039/9781849739955-00087

[28] A. W. Walker, O. Theriault, *et al.,* Carrier dynamics in Quantum-Dot multijunction solar cells under concentration, *IEEE Journal of Photovoltaics*, 4, 1095–1099, *(2014)*. https://doi.org/10.1109/jphotov.2014.2322279

[29] D.J. Friedman, Progress and challenges for next-generation high-efficiency multijunction solar cells, *Current Opinion in Solid State and Materials Science,* 14, 131-138, *(2010).* https://doi.org/10.1016/j.cossms.2010.07.001

[30] Lomas, A. D. U, *Tuning the properties of InAs/GaAs quantum dots through a modified capping layer: Application to optoelectronic devices, Doctoral Thesis, Universidad Politecnica de Madrid, (2017).* https://doi.org/10.20868/upm.thesis.47348

[31] J. Zhu, K. Lu, *et al.,*. Tandem Solar Cells based on Quantum Dots, *Materials Chemistry Frontiers*. *(2024)*. https://doi.org/10.1039/d3qm01087b

[32] G. Landis, S. Bailey, Photovoltaic power for future NASA missions. *American Institute of Aeronautics & Astronautics, (2002)*. https://doi.org/10.2514/6.2002-718

[33] S. Bailey, G. Landis, The next-generation of space cells for diverse environments, *Proceedings of the 6th European Conference on Space Power*, Porto (Portugal), *(2002).* https://doi.org/10.2514/6.2002-718

[34] K.K. de Groh, B. A. Banks, Environmental Durability Issues for Solar Power Systems in Low Earth Orbit, *NASA Technical Memorandum, (I995): https://ntrs.nasa.gov/api/citations/19950009355/downloads/19950009355.pdf*

[35] P. A. Iles, Photovoltaic Conversion: space applications, *Encyclopedia of Energy,* 25–33, *(2004)*. https://doi.org/10.1016/b0-12-176480-x/00332-6

[36] A. I. Fedoseyev *et al*., Investigation and modeling of space radiation effects in quantum dot solar cells, *35th IEEE Photovoltaic Specialists Conference*, Honolulu, 2533-2536, *(2010)*. https://doi.org/10.1109/PVSC.2010.5614621

[37] Z. S. Bittner, H. Kum, *et al.,* Integration of Quantum Dots and Quantum Wells into InGaAs Metamorphic Subcell for Radiation Hard 3-J ELO IMM Photovoltaics, *IEEE 44th Photovoltaic Specialist Conference (PVSC), (2017)*. https://doi.org/10.1109/pvsc.2017.8366357

[38] T. Soga, Fundamentals of Solar Cell, *Nanostructured Materials for Solar Energy Conversion*, 3 - 43, *(2006)*. https://doi.org/10.1016/b978-044452844-5/50002-0

[39] D. Cote, Generating, controlling and time-resolving ultrafast photocurrents in GaAs, *Doctoral Thesis, University of Toronto, (2003).*

[40] Facts.net: https://facts.net/science/chemistry/10-astonishing-facts-about-p-n-junction/

[41] K. Bhaskar, Zinc Cadmium Sulphide And Zinc Sulphide As Alternative Heterojunction Partners For Cigs2 Solar Cells, *Master Thesis, (2007)*. https://stars.library.ucf.edu/etd/3234

[42] PVEducation: https://www.pveducation.org/pvcdrom/solar-cell-operation/open-circuit-voltage

[43] T. Markvart, L. Castañer, McEvoy's Handbook of Photovoltaics (Third Edition), *Fundamentals and Applications, (2018)*. https://doi.org/10.1016/b978-0-12-809921-6.00001-x

[44] M.A. Green, Solar Cells: Operating Principles Technology and System Applications, *(1982)*.

[45] N. Miyashita, N. Ahsan, *et al.,* Generation and collection of photocarriers in dilute nitride GaInNAsSb solar cells*, Progress in Photovoltaics: Research and Applications,* 24, 28-37, (*2015*). https://doi.org/10.1002/pip.2641

[46] T.W. Kim, K. Forghani *et al.,* Properties of 'bulk' GaAsSbN/GaAs for multi-junction solar cell application: Reduction of carbon background concentration, *Journal of Crystal Growth*, 393, 70-74, *(2014)*. https://doi.org/10.1016/j.jcrysgro.2013.10.034

[47] M. Schwarz; A. G. Carro, Unintentional Doping in GaAsSb/GaAsN Superlattice Solar Cells, *14th Spanish Conference on Electron Devices (CDE)*, Valencia, Spain, 2023, 1-4. https://doi.org/10.1109/CDE58627.2023.10339430

[48] I. Sychugov, Synthesis and Properties of Single Luminescent Silicon Quantum Dot, *Doctoral Thesis, KTH Royal Institute of Technologies, (2006)*.

[49] L. Brus, Electronic wave functions in semiconductor clusters: experiment and theory, *Journal of Physical Chemistry*, 90, 2555–2560*, (1986).* https://doi.org/10.1021/j100403a003

[50] F.P.G De Arquer, D.V. Talapin, *et al*., Semiconductor quantum dots: Technological progress and future challenges, *Science*, *373*, *(2021)*. https://doi.org/10.1126/science.aaz8541

[51] A. C. Dinesh, Introduction to Nanoscience and Nanomaterials || Semiconductor quantum dots. Semiconductor quantum dots., *World Scientific,* 117 – 139 *(2013)*. https://doi.org/10.1142/9789814397988_0004

[52] L. N. McCabe, J. M. O. Zide, Techniques for epitaxial site-selective growth of quantum dots, *Journal of Vacuum Science & Technology. A. Vacuum, Surfaces, and Films*, 39, *(2020).* https://doi.org/10.1116/6.0000623

[53] P. Yu, Z. M. WangQuantum Dot Optoelectronic Devices, *Lecture notes in nanoscale science and technology*, *(2020).* https://doi.org/10.1007/978-3-030-35813-6

[54] I. Shibasaki, N. Kuze,Mass production of sensors grown by MBE, *Molecular Beam Epitaxy,* 697 – 720 , *(2013)*. https://doi.org/10.1016/b978-0-12-387839-7.00031-2

[55] A. Cho, J. Arthur, Molecular beam epitaxy, *Progress in Solid State Chemistry/Progress in Solid State Chemistry*, *10*, 157–191, *(1975)*. https://doi.org/10.1016/0079-6786(75)90005-9

[56] A. Bhattacharya, B. Bansal, Self-Assembly in semiconductor epitaxy, *Handbook of Crystal Growth (Second Edition)*, 1057–1099, *(2015)*. https://doi.org/10.1016/b978-0-444-63304-0.00026-3

[57] A. Nemcsics, A. (2015). Quantum dots prepared by Droplet epitaxial Method, *Quantum Dots - Theory and Applications, (2015)*. https://doi.org/10.5772/60823

[58] E. Bauer, Phenomenological theory of crystal deposition on surfaces, *Journal of Crystallography - Crystalline Materials*, 110, 372–394, *(1958)*. https://doi.org/10.1524/zkri.1958.110.1-6.372

[59] Y. H. Zhang, D. J. Smith, Heterovalent semiconductor structures and devices grown by molecular beam epitaxy, *Journal of Vacuum Science and Technology A*, 39, 030803, *(2021)*. https://doi.org/10.1116/6.0000802

[60] M. V. Rakhlin, K.G. Belyaev, *et al.,* InAs/AlGaAs quantum dots for single-photon emission in a red spectral range, *Scientific Reports*, 8, *(2018)*. https://doi.org/10.1038/s41598-018-23687-7

[61] D. Bimberg, *Semiconductor nanostructures*, *Springer, (2008)*.

[62] J. M. Ulloa, R. Gargallo-Caballero, *et al.,* GaAsSb-capped InAs quantum dots: From enlarged quantum dot height to alloy fluctuations, *Physical Review. B, Condensed Matter and Materials Physics*, 81, *(2010)*. https://doi.org/10.1103/physrevb.81.165305

[63] Kim, Y., Cho, I. W., Ryu, M. Y., Kim, J. O., Lee, S. J., Ban, K. Y., & Honsberg, C. (2017). Stranski–Krastanov InAs/GaAsSb quantum dots coupled with sub-monolayer quantum dot stacks as a promising absorber for intermediate band solar cells. *Applied Physics Letters*, *111*(7). https://doi.org/10.1063/1.4999437

[64] Joyce, B. A., & Vvedensky, D. D. (2005b). Quantum Dots in the InAs/GaAs System. In *Quantum Dots: Fundamentals, Applications, and Frontiers* (pp. 1–26). https://doi.org/10.1007/1-4020-3315-x_1

[65] Saito, H., Nishi, K., & Sugou, S. (1999). Shape transition of InAs quantum dots by growth at high temperature. *Applied Physics Letters*, *74*(9), 1224–1226. https://doi.org/10.1063/1.123506

[66] S. Ozdemir, Y. E. Suyolcu, *et al.,* Influence of the growth conditions on the optical and structural properties of self-assembled InAs/GaAs quantum dots for low As/In ratio. *Applied Surface Science*, 392, 817–825, *(2017)*. https://doi.org/10.1016/j.apsusc.2016.08.162

[67] A. D. Utrilla, D.F. Grossi, *et al.,* Size and shape tunability of self-assembled InAs/GaAs nanostructures through the capping rate. *Applied Surface Science*, 444, 260–266, *(2018)*. https://doi.org/10.1016/j.apsusc.2018.03.098

[68] J. G. Keizer, J. M. Ulloa, *et al.,* InAs quantum dot morphology after capping with In, N, Sb alloyed thin films, *Applied Physics Letters*, 104, *(2014)*. https://doi.org/10.1063/1.4864159

[69] O. Schumann, S, Birner, *et al.,* Effects of strain and confinement on the emission wavelength of InAs quantum dots due to a$GaAs_{1-x}N_x$ capping layer, *Physical Review B, Condensed Matter and Materials Physics*, 71, *(2005)*. https://doi.org/10.1103/physrevb.71.245316

[70] D. González, S. Flores, Evaluation of different capping strategies in the InAs/GaAs QD system: Composition, size and QD density features, *Applied Surface Science*, *537*, 148062, *(2021)*. https://doi.org/10.1016/j.apsusc.2020.148062

[71] J. M. Ulloa, I. W. D. Drouzas, *et al.,* Suppression of InAs/GaAs quantum dot decomposition by the incorporation of a GaAsSb capping layer, *Applied Physics Letters,* 90*,* https://doi.org/10.1063/1.2741608

[72] W. Liu, C. Chang, Capping InAs quantum dots with an InGaAsSb strain-reducing layer to improve optical properties and dot-size uniformity, *Thin Solid Films*, 570, 490–495, *(2014)*. https://doi.org/10.1016/j.tsf.2014.04.032

[73] J. M. Ulloa, J. M. Llorens, *et al.,* Analysis of the modified optical properties and band structure of $GaAs_{1-x}Sb_x$-capped InAs/GaAs quantum dots, *Journal of Applied Physics*, 112, *(2012)*. https://doi.org/10.1063/1.4755794

[74] J. M. Ulloa, D. F. Reyes, Independent tuning of electron and hole confinement in InAs/GaAs quantum dots through a thin GaAsSbN capping layer. Applied Physics Letters, 100 (2012). http://dx.doi.org/10.1063/1.3673563

[75] Dai, C. G. Bailey, C. Kerestes, D. V. Forbes and S. M. Hubbard, Investigation of carrier escape mechanism in InAs/GaAs quantum dot solar cells, *2012 38th IEEE Photovoltaic Specialists Conference*, Austin, TX, USA, 2012, 39-44. https://doi.org/10.1109/PVSC.2012.6317564

[76] Ru, E. C. L., Fack, J., & Murray, R. (2003). Temperature and excitation density dependence of the photoluminescence from annealed InAs/GaAs quantum dots. *Physical Review. B, Condensed Matter*, *67*(24). https://doi.org/10.1103/physrevb.67.245318

[77] A. D. Utrilla, D. Reyes, *et al.,* Thin GaAsSb capping layers for improved performance of InAs/GaAs quantum dot solar cells, *Solar Energy Materials & Solar Cells/Solar Energy Materials and Solar Cells*, 159, 282–289, *(2017).* https://doi.org/10.1016/j.solmat.2016.09.006

[78] X. J. Shang, J. F. He, *et al.,* Effect of built-in electric field in photovoltaic InAs quantum dot embedded GaAs solar cell. *Applied Physics. A, Materials Science & Processing*, 103, 335–341, *(2010)*. https://doi.org/10.1007/s00339-010-6152-8

[79] A. Luque, A. Martí, The intermediate band solar cell: progress toward the realization of an attractive concept. *Advanced Materials*, 22, 160–174, *(2009)*. https://doi.org/10.1002/adma.200902388

[80] D. Zhou, G. Sharma, *et al.*, Optimization towards high density quantum dots for intermediate band solar cells grown by molecular beam epitaxy, *Applied Physics Letters*, 96, *(2010)*. https://doi.org/10.1063/1.3313938

[81] F. K. Tutu, J. Wu, *et al.,* Antimony mediated growth of high-density InAs quantum dots for photovoltaic cells, *Applied Physics Letters,* 103*, (2013).* *https://doi.org*/doi:10.1063/1.4816503

[82] N. Ruiz-Marín, D.F. Reyes, *et al.,* Effect of the AlAs capping layer thickness on the structure of InAs/GaAs QD, *Applied Surface Science*, 573, *(2022).* https://doi.org/10.1016/j.apsusc.2021.151572

[83] H. Liang, F. Wang, *et al.,* Progress in full spectrum solar energy utilization by spectral beam splitting hybrid PV/T system, *Renewable & Sustainable Energy Reviews*, *141*, 110785, *(2021)*. https://doi.org/10.1016/j.rser.2021.110785

[84] J. Bisquert, The Physics of Solar Cells Perovskites: Organics, and Photovoltaic Fundamentals, *CRC Press, Taylor & Francis Group, (2018).* https://lccn.loc.gov/2017029026

[85] Standard ASTM E490-00a, Standard solar constant and zero air mass solar spectral irradiance tables, *ASTM International*, West Conshohocken PA *(2014).*

[86] Standard ASTM G173-03, Standard tables for reference solar spectral irradiances: direct normal and hemispherical on 37° tilted surface, *ASTM International*, West Conshohocken PA *(2012).*

[87] J. Fieducik, The use of solar radiation for generating heat in a solar air collector in northern Poland, *E3S Web of Conferences*,100, *(2019).* https://doi.org/10.1051/e3sconf/2019100000

[88] PVEducation: https://www.pveducation.org/pvcdrom/appendices/standard-solar-spectra

[89] H. F. Lu, L. Fu, *et al.*, Temperature dependence of dark current properties of InGaAs/GaAs quantum dot solar cells, *Applied Physics Letters*, 98, *(2011).* https://doi.org/10.1063/1.3586251

[90] S. Kondratenko, A. Yakovliev, *et al.,* Influence of built-in charge on photogeneration and recombination processes in InAs/GaAs quantum dot solar cells, *Journal of Physics. D, Applied Physics*, 50, 165101, *(2017)*. https://doi.org/10.1088/1361-6463/aa61d4

[91] H. Kim, M. Park, *et al.,* Influence of InAs quantum dots on the transport properties of GaAs-based solar cell devices, *Current Applied Physics*, 14, 192–195, *(2014)*. https://doi.org/10.1016/j.cap.2013.11.003

[92] A.D. Utrilla, J.M. Ulloa, *et al.,* Impact of alloyed capping layers on the performance of InAs quantum dot solar cells, *Solar Energy Materials & Solar Cells,* 144, 128-135, *(2016)*. https://doi.org/10.1016/j.solmat.2015.08.009

[93] Y. Kim, K. Ban, *et al.*, Material and device characteristics of InAs/GaAsSb sub-monolayer quantum dot solar cells, *Applied Physics Letters*, 107, *(2015)*. https://doi.org/10.1063/1.4933272

[94] W. Liu, H. Wu, *et al.,* Improving the characteristics of intermediate-band solar cell devices using a vertically aligned InAs/GaAsSb quantum dot structure, *Solar Energy Materials & Solar Cells/Solar Energy Materials and Solar Cells*, 105, 237–241, *(2012).* https://doi.org/10.1016/j.solmat.2012.06.023

[95] Y. Cheng, A. J. Meleco, *et al.,* An Investigation of the Role of Radiative and Nonradiative Recombination Processes in InAs/$GaAs_{1-x}Sb_x$ Quantum Dot Solar Cells, *IEEE Journal of Photovoltaics*, 8, 487–492, *(2018)*. https://doi.org/10.1109/jphotov.2017.2779325

[96] Y. D. Jang, T. J. Badcock, *et al.,* Carrier lifetimes in type-II InAs quantum dots capped with a GaAsSb strain reducing layer, *Applied Physics Letters*, 92, 251905 *(2008).* https://doi.org/10.1063/1.2949741

[97] D. J. Dumin, G. L. Pearson, Properties of Gallium Arsenide diodes between 4.2 and 300 K, *J. Appl. Phys.*, 36, 3418–3426, *(1965)*. https://doi.org/10.1063/1.1703009

[98] M. Lee, H. Lee, *et al.,* Investigation of Forward Tunneling Characteristics of InGaN/GaN Blue Light-Emitting Diodes on Freestanding GaN Detached from a Si Substrate, *Nanomaterials*, 8, 543, *(2018)*. https://doi.org/10.3390/nano8070543

[99] D. Yan, H. Lu, *et al.,* Forward tunneling current in GaN-based blue light-emitting diodes. *Applied Physics Letters*, 96, *(2010)*. https://doi.org/10.1063/1.3327332

[100] A. Kaminski, J. Marchand, *et al.,* Non ideal dark I–V curves behavior of silicon solar cells, *Solar Energy Materials & Solar Cells/Solar Energy Materials and Solar Cells*, 51, 221–231, *(1998)*. https://doi.org/10.1016/s0927-0248(97)00216-x

[101] G. Jolley, H. Lu, *et al.,* Electron-hole recombination properties of In0.5Ga0.5As/GaAs quantum dot solar cells and the influence on the open circuit voltage, *Applied Physics Letters*, 97, *(2010)* https://doi.org/10.1063/1.3492836

[102] W. K. Loke, S. F. Yoon, *et al.,* Defect-induced trap-assisted tunneling current in GaInNAs grown on GaAs substrate, *Journal of Applied Physics*, 112, *(2007).* https://doi.org/10.1063/1.2775908